MASTERARBEIT | MASTER'S THESIS

Titel | Title

Towards a Device Independent Measurement of Indefinite Causal Order with a Quantum SWITCH

verfasst von | submitted by

Carla Maria Davida Richter BSc

angestrebter akademischer Grad | in partial fulfilment of the requirements for the degree of

Master of Science (MSc)

Wien | Vienna, 2024

Studienkennzahl lt. Studienblatt | Degree programme code as it appears on the student record sheet:	UA 066 876
Studienrichtung lt. Studienblatt | Degree programme as it appears on the student record sheet:	Masterstudium Physics
Betreut von | Supervisor:	Univ.-Prof. Dipl.-Ing. Dr. Philip Walther
Mitbetreut von | Co-Supervisor:	Lee Arthur Rozema BSc (Hons) PhD

Acknowledgements

As I reflect on the journey that led to the completion of this thesis, I am reminded of the many individuals whose support and encouragement have been invaluable over the past few years. I would like to take this opportunity to express my gratitude to everyone who has been there for me along the way. Although this appreciation often remains unspoken, it is always in my thoughts.

To begin with, I want to thank Prof. Walther, who welcomed me into his research group and provided me with the extraordinary opportunity to participate in research even before the start of my master's studies. This opportunity has granted me valuable insight into the research field, which is often beyond the reach of students, and I sincerely appreciate the additional depth it has brought to my education. Being part of a team that is at the forefront of innovative research and filled with kind and supportive colleagues has truly been a privilege.

I'd also like to give a special thanks to to Lee Rozema for being such a supportive supervisor. His guidance throughout this journey has been invaluable. Always ready to patiently address my questions, he helped me navigate any challenges that arose during the project. Consistently focusing on my concerns when needed, he never dismissed any issue as too minor or trivial. All the support he provided along the way is something I truly appreciate.

I would be remiss not to thank Michael Antesberger for his constant help. Whenever I faced a problem in the lab, he was always ready to lend a hand. His willingness to explain experimental methods clearly and dedicate significant time to show me better ways to tackle issues made a big difference. Everything he did to support me has been invaluable.

Additionally, I want to acknowledge Philipp Jenke for teaching me so much about programming, which made it easier for me to carry out measurements and analyse data effectively.

Essentially, I have to thank everyone from the fourth floor for being such a lovable crew who could always cheer me up and keep things entertaining, even during those moments when the lab wasn't cooperating.

Lastly, I want to mention those who are closest to me and have supported me throughout my life and now also through my studies. Lukas has always been there for me, a reliable presence I can turn to, and he encourages me to question what I might otherwise take for granted. My sister Pia, who started studying physics alongside me, was such a great support that she helped me survive the first semesters. And my father, Andreas, who sparked my interest in physics from a young age has been pivotal in my journey; without him, I would never have started this.

Abstract

In the realm of quantum mechanics, processes can exhibit undefined causal order, calling into question the fundamental principles of classical causality. This field of indefinite causal order (ICO) has received growing attention in recent years, particularly due to the experimental realisation of the quantum SWITCH. Nonetheless, it remains a work in progress to provide conclusive proof that these experimental setups truly create indefinite causal orders and exclude alternative explanations for the investigated results. Recently, van der Lugt et al. [1] introduced a local causal inequality that can be broken by the quantum SWITCH. This opens the door for the first device-independent demonstration of the indefinite causal order of quantum channels in the experimental SWITCH.

The aim of this master thesis was to build an experimental setup that is capable to demonstrate the violation of this inequality and to test it's performance through preliminary measurements.

Two-qubit quantum state tomography was used to test whether the setup allows for sufficiently precise measurements and if the polarisation state, generated in the down-conversion source, corresponds to the pure entangled state required for the experiment. In order to evaluate the performance of the quantum switch, the commutation game was performed. This involves a series of measurements where two commuting or anticommuting operators are implemented within the SWITCH. The goal is to determine which case applies by calling each gate only once. In this work, the setup and its functionality will be described in detail following an overview of the theoretical background on indefinite causal order, the quantum switch, and the local causal inequality. The results from preliminary measurements will then be presented, along with a discussion of how they offer promising prospects for successfully realising the violation of the local causal inequality.

Zusammenfassung

Die Quantenmechanik erlaubt Prozesse mit undefinierter kausaler Reihenfolge, die die grundlegenden Prinzipien der klassischen Kausalität infrage stellen. Dieses Gebiet der *indefinite causal order* (ICO) hat in den letzten Jahren immer mehr Aufmerksamkeit gewonnen, insbesondere durch den sogenannten Quanten-Switch – ein ICO-Prozess, der sich im Labor realisieren lässt. Es bleibt jedoch eine Herausforderung, eindeutig nachzuweisen, dass dieser experimentelle Switch tatsächlich undefinierte kausale Ordnungen erzeugt und alternative Erklärungen ausgeschlossen werden können. Kürzlich wurde von van der Lugt et al. eine lokale kausale Ungleichung veröffentlicht[1] , die vom Quanten-Switch gebrochen werden kann. Damit eröffnet sich die Möglichkeit zur ersten geräteunabhängigen Demonstration der ICO im experimentellen Switch. Das Ziel dieser Masterarbeit war es, ein optisches Experiment aufzubauen, das die Brechung dieser kausalen Ungleichung erlaubt und dessen Leistung in Testmessungen zu evaluieren.
Mittels Tomographien des Quantenzustands sollte überprüft werden, ob der Aufbau ausreichend präzise Messungen ermöglicht und ob der in der Down-Conversion-Quelle erzeugte Polarisationzustand dem für das Experiment erforderlichen reinen, verschränkten Bell-Zustand entspricht. Zur Testung des Quanten-Switch wurde das sogenannte *Commutation game* durchgeführt. Dabei werden zwei kommutierende oder antikommutierende Operatoren im Switch ausgeführt. Ziel ist es, mit nur einem Durchlauf durch das Experiment zu bestimmen, in welcher dieser beiden möglichen Beziehungen die Operatoren zueinander stehen. Im folgenden Text werden Aufbau und Funktionsweise des Experiments ausführlich beschrieben, beginnend mit einem Überblick über die theoretischen Hintergründe zur ICO, dem Quanten-Switch und der lokalen kausalen Ungleichung. Anschließend werden die Ergebnisse aus den Testmessungen präsentiert, zusammen mit einer Diskussion darüber, inwiefern sie Grund zu Optimismus geben, dass mit dem Experiment eine erfolgreiche Brechung der Ungleichung möglich sein wird.

Contents

1 Indroduction

Early on, the peculiarities of quantum mechanics prompted physicists to consider whether assumptions about temporal order also require rethinking. As an example, in his 1951 article 'Zur Frage der Kausalität in der Quantentheorie der Elementarteilchen' (On the Question of Causality in the Quantum Theory of Elementary Particles), Heisenberg describes a certain particle decay processes that leave open the possibility that a particle created during a collision might have already decayed before the collision occurred. Furthermore, he speculates about physical processes that could only become possible through the suspension of classical causal orders [2].
Nonetheless, such considerations remained strictly theoretical, existing in the background and far removed from robust theoretical analysis and even further from experimental verification. Therefore, the scientific view up until a few years ago relied on the common agreement that time runs in a defined and certain direction, resulting in a global causal structure. However, this view can no longer be upheld, as recent findings have shown that quantum theory allows for scenarios with indefinite causal order (ICO).
A defined causal order exists when it can be clearly stated that an action in the past influences an action in the future but not vice versa. For example, if someone measures a quantum system and prepares it in a new state, this will affect the outcome of a subsequent measurement on the system. Such situations, as well as probabilistic mixtures of defined causal orders, rely on classical descriptions of time. However, similar to spatial superposition, a quantum system can exist in a superposition of different causal orders, leading to a causally non-separable process [3]. The quantum SWITCH is one such process that can create an ICO. In the SWITCH, the order of operations is determined by the state of a control qubit. When the control qubit is in superposition, the order of operations is similarly superposed. What makes the quantum SWITCH particularly significant is that it can be experimentally realised, and this has been demonstrated in several experiments over the past few years. The first experimental demonstration was carried out in 2015 by Procopio et al.[4]. They showed that certain tasks can be performed more efficiently using an ICO. Specifically, it was demonstrated that the quantum SWITCH can distinguish between commuting and anticommuting unitary operators with just a single use of each operator. In contrast, classical methods would require to apply each gate at least twice to substantiate this claim. The measurements that demonstrated this capability are referred to as "the commutation game".
Already this result indicated that the interest in ICO is not only be justified by fundamental questions, yet that it may also provide applicably advantages in quantum information tasks. It has been theoretically and experimentally shown, that communication threw noisy channels can be significantly enhanced by the use of a quantum SWITCH [5][6]. Furthermore is has been demonstrated that ICO can improve the estimation precision in quantum metrology [7].While there is no evidence so far that incorporating ICO provides

a general advantage beyond quantum computing with a defined order of operations, it does enable a broader approach to quantum computing that cannot be captured within the conventional quantum circuit model [8][9].
Despite the strong experimental results, there is still a debate over whether the experimental SWITCH indeed creates an ICO, and a key task that remains is to find a device-independent way to prove this. Such a proof would be a strong confirmation of the ICO, much like Bell tests provide evidence for entanglement. However, it has been shown that this cannot be achieved through causal inequalities of the kind discussed in recent years [10]. Most of the earlier evidence for indefinite causal order in the quantum SWITCH, such as the measurement of causal witness by Rubino et al. in 2017 [11], relies on assumptions about the underlying quantum system. Stronger evidence came from a theory-independent approach by Rubino et al. in 2022 [12], which demonstrated the effect without relying on quantum formalism, using only probabilities. However, these probabilities still depend on assumptions about the state and the operations on that state. A semi-device-independent proof was later provided by Cao et al. in 2023 [13]. This semi-device-independent inequality involved three parties but required assumptions only about the operations of one of them.
Recently, van der Lugt et al. [1] presented a new type of causal inequality that offers the potential for the quantum SWITCH to violate it, pushing the boundaries of previous approaches. This would finally allow for device-independent verification of the quantum SWITCH. This local causal inequality relies only on assumptions about definite causal order and relativistic causality, without requiring assumptions about the process or underlying operations.
The objective of this Master's thesis is to construct and test a setup capable of measuring and violating this local causal inequality, providing the first device-independent evidence of the ICO in a quantum SWITCH. The quantum SWITCH in this setup is a time-bin-controlled, fibre-based SWITCH that utilises the superposition of the temporal degree of freedom to create a superposition of the order in which operators are applied to a polarisation target qubit. This type of SWITCH was previously used by Antesberger et al. to measure the process matrix of the quantum SWITCH [14]. Compared with previous implementations of the quantum SWITCH based on path-encoded control qubits [11][4], this type of SWITCH has the advantage of being passively stable, allowing measurements over longer time periods without the need for active stabilisation, as it was done by Cao et al.[13]. After constructing and ensuring the correct functioning of the setup, it was tested by implementing the commutation game, with an entangled control photon. A single-photon down-conversion source was used to generate an entangled Bell state. One of the photons was measured such that it projected the required diagonal polarisation onto the photon sent into the SWITCH setup.
Since we utilize a novel technique for measuring the control qubit, we want to benchmark the performance of the implemented SWITCH by conducting the commuation game. We expect that if the setup can successfully measure the commutation game, including entanglement, it will also be capable of violating the local causal inequality.
In this thesis, I will provide an overview of the required theory for ICO, the quantum

SWITCH, and the local causal inequality. Additionally, I will describe the setup and its functionality, with a focus on key elements such as the single-photon source and the creation of the time-bin control qubit. The necessary experimental methods for polarisation compensation, two-qubit tomography, and the commutation game will also be addressed. Finally the experimental result will be presented and discussed together with the further steps towards the measurement of the local causal inequality.

2 Theoretical Background

This chapter outlines the theoretical framework for the study, divided into three sections. It begins with the concept of indefinite causal order, discussing the difference between classical temporal orders and causally inseparable processes and providing a brief overview of the causal inequality proposed by Oreshkov et al. [3].
The second section focuses on the Quantum Switch, which is a particular causally inseparable process, and how it works, It also includes a subchapter on the Commutation Game experiment, which is the first application of the Quantum Switch. The final section discusses the theory of the Local Causal Inequality [1]. The goal of this thesis is to build an experiment capable of violating this inequality.

2.1 The General Concept of Indefinite Causal Order

This section describes the concept of indefinite causal order, following Oreshkov et al.'s paper "*Quantum Correlations with No Causal Order*". [3].
To clarify what is meant by causal orders and the conditions under which they become undefined, let's consider the following scenario: two parties, Franz (F) and Louis (L), are situated in isolated laboratories representing event locations. We can define the causal order by the allowed signalling: If Franz can signal to Louis, it is permitted, that Louis signals back to Franz and thereby it is clearly defined, that Franz is in the causal past of Louis. Vice versa, if Louis can signal to Franz.
An example of such a process, would be a situation, in which Louis measures and prepares a quantum state of a two-level system and then sends it afterwards to Franz, who can also measure and prepare it, but can't send it back to Louis. Such a situation can be symbolised with F$\npreceq$L. To describe of signalling probabilities between two parties, the of process matrix formalism was introduced:
A completely positive (CP) trace-non-increasing map $\mathcal{M}_j^F = \mathcal{L}(\mathcal{H}^{F_1}) \rightarrow \mathcal{L}(\mathcal{H}^{F_2})$ represents the transformation from an input to an output $j = 1...n$ over the space of matrices $\mathcal{L}(\mathcal{H}^{F_1}), \mathcal{L}(\mathcal{H}^{F_2})$, with Franz's input and output Hibertspaces $\mathcal{H}^{F_1}$ and $\mathcal{H}^{F_2}$. Such a map $\mathcal{M}_j$ can represent any kind of process including unitary evolution and measurements. In this example it describes a measurement with the outcome j. Considering an input quantum state represented by a density matrix ρ the CP-map $\mathcal{M}_j^F$ allows us to calculate the updated state $\mathcal{M}_j^F(\rho)$ up to its normalisation and its probability of outcome $P(\mathcal{M}_j^F) = \mathrm{Tr}\left[\mathcal{M}_j^F(\rho)\right]$.
Furthermore, Oreshkov et al. showed that, via the Choi-Jamiołkowsky (CJ) isomorphism, such CP-maps can be represented by positive-semidefinite matrices (CJ-Matrices). Thus, the CP-map $\mathcal{M}_i = \mathcal{L}(\mathcal{H}^{F_1}) \rightarrow \mathcal{L}(\mathcal{H}^{F_2})$ can be described as the matrix $M_i^{F_1F_2}$ via the definition $M_i^{F_1F_2} := \mathbb{1} \otimes \mathcal{M}_i \left[|\psi^+\rangle\langle\psi^+|\right]^T$, with the unnormalised, maximally entangled

state $|\psi^+\rangle = \sum_{j=1}^{d_{F_1}} |jj\rangle \in \mathcal{H}^{F_1} \otimes \mathcal{H}^{F_2}$, where $d_{F_1} = \dim(\mathcal{H}^{F_1})$, and $\mathbb{1}$ is the identity matrix. With these tools, we can now to describe quantum experiments with a defined input and output, but without any assumptions about the preexisting background time and the causal order between different parties.
Going back to the initial idea of the two agents Franz (F) and Louis (L), the probability of two measurement outcomes i, j in two closed laboratories can now be expressed as:

$$P(\mathcal{M}_i^F, \mathcal{M}_j^L) = Tr\big[\ W^{F_1F_2L_1L_2}\big(\ M_i^{F_1F_2} \otimes M_j^{L_1L_2}\big)\big] \tag{2.1}$$

With the semidefinite matrix $W^{F_1F_2L_1L_2}$ in $\mathcal{L}(\mathcal{H}^{F_1} \otimes \mathcal{H}^{F_2} \otimes \mathcal{H}^{L_1} \otimes \mathcal{H}^{L_2})$. Under the premise that $\mathcal{M}^F$ and $\mathcal{M}^L$ are completely positive and trace-preserving, and that all probabilities of W are non-negative and sum up to 1, $W^{F_1F_2L_1L_2}$ represents a process matrix.
Such a process matrix can be seen as a generalisation of a density matrix that describes the probabilities of a bipartite process in local quantum mechanics. The example $W^{F_1F_2L_1L_2}$ in eq. 2.1 describes connections between Franz and Louis. These connections can now be specified such that they define a clear causal order without any assumptions on the background time. For example, if Franz performs a measurement on his system and then sends it to Louis, Franz is inevitably in Louis' causal past, as Louis cannot signal back to Franz without violating the rule that each party receives only one system per round.
So if there is a probability p that Franz can't signal to Louis ($F \npreceq L$) and a probability $(1-p)$ that Louis can't signal to Franz ($L \npreceq F$), then this situation can be described as a causal separable state via the process matrix.

$$W^{F_1F_2L_1L_2} = pW^{F \npreceq L} + (1-p)W^{L \npreceq F} \tag{2.2}$$

Since here the matrix can be written in two separate terms, one representing the scenario in which Louis is in the causal past of Franz and the other representing the opposite. We can interpret $W^{F_1F_2L_1L_2}$ here as a classical mixture of these two processes. A causal inseparable process requires a coherent superposition of these two orders.
Oreshkov et al. demonstrated in their paper [3] that they can find process matrices that satisfy all requirements of a bipartite process but are nevertheless inseparable. In local quantum mechanics, no causal order can be defined for such a process. Thus, it is impossible to determine whether Franz is in the causal past of Louis or vice versa.
Let's now imagine that Franz and Louis are each sitting in their own closed laboratories, playing a game. In each round of the game, they both receive a two-level quantum system on which they can perform operations, such as measurements or rotations on the spin, before sending it out of their laboratory. Aside from these systems, no information can leak into or out of their laboratories.

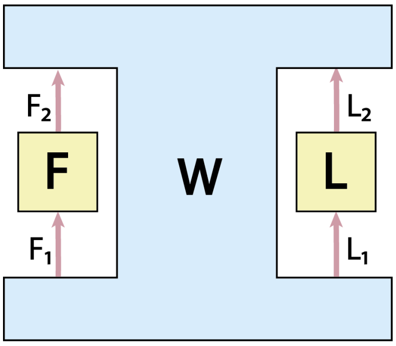

Figure 2.1: **Representation of a bipartite process matrix W:** in this examples it connects the input systems F_1, L_1 to the output systems F_2, L_2. [10]

As a second rule of the game, both Louis and Franz have to toss a coin once they have received the physical system, which gives them a random bit, named f or l (depending on who tosses the coin) and two other bits denoted as x and y. Additionally, Louis generates a third bit $l' \in 0, 1$ that determines how this round of the game is won.
If he gets the bit $l' = 0$, Franz must output Louis bit such that $x = l$, while if $l' = 1$ Louis must output Franz's bit $y = f$.
Franz and Louis win the game when their outputs x, y are correct; therefore, they must maximise their probability of success:

$$P_{succ} := \frac{1}{2}\left[\, P(x = l \mid l' = 0) + P(y = f \mid l' = 1)\right] \tag{2.3}$$

The probability of each party to make the right guess of y or x is influenced by the causal order in which they operate. Thus, the optimal strategy requires the player in the causal past to encode information about his bit in the physical system, which is later measured by the player in their causal future. For example, consider Franz in the causal past of Louis. If $l' = 1$, Louis must guess Franz's bit f, they can achieve $P(y = f \mid l' = 1) = 1$. However, with $l' = 0$, Franz is forced to guess l randomly, resulting in $P(x = l \mid l' = 0) = 0.5$.
Thus, the probability of success is constrained by the causal inequality:

$$P_{succ} \leqslant \frac{3}{4} \tag{2.4}$$

However, Oreshkov et al. were able to show that causally inseparable processes, like that discovered by Oreshkov et a., can exceed this boundary, meaning that Franz and Louis could increase their chances of winning the game beyond the classical limit by accessing a process with indefinite causal order.
Unfortunately, to this day, no known process with an indefinite causal order can be experimentally implemented and break this type of causal inequality. Instead all existing experimental demonstrations of ICO have been device dependent [1].

2.2 The Quantum SWITCH

The quantum-SWITCH was first described in 2013 by Chiribella et al. in their paper *"Quantum Computations without Definite Causal Structure"* [15]. Together with the "quantum time flip"[16] the quantum Switch is the only process with indefinite causal order that has been experimentally realised [17].
The concept originated from the idea of a machine with movable wires and two physical boxes
[f] and **[g]**. Via a control qubit the wires are moved in such way, that they change the order of these boxes. For the control-qubit in $|0\rangle_C$ the wires are placed so that **[g]** is reached first and **[f]** afterwards. For the control qubit in $|1\rangle_C$ the order of these boxes is reversed.
If one could allow these wires to be superposed and place the control qubit in a superposition state of $|0\rangle_C$ and $|1\rangle_C$, this would create entanglement between the microscopic control system and the macroscopic system of the wires. This quantum-controlled device has an ICO and can not be represented by a classical quantum circuit [15].

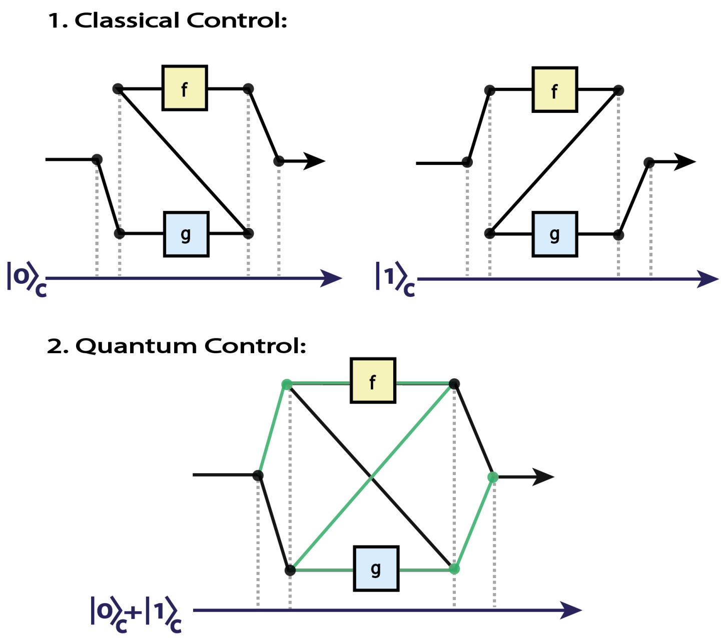

Figure 2.2: **The program SWITCH:** 1. For a classical control over the movable wires, the order of the boxes **[f]** and **[g]** is clearly defined. 2. The quantum SWITCH: a quantum control qubit in a superposition allows a superposition of the order of the boxes. [15]

The quantum SWITCH was the first process of indefinite causal that was demonstrated experimentally [4] and is now considered "the canonical example of a Quantum Circuit with Quantum Control of causal order (QC-QC) " [18, p. 20]. However, since it is challenging to place movable wires in a superposition, all existing experimental implementations of the quantum SWITCH use photons in superposition of different modes, such as time and path [4][17]. The process matrix of the quantum SWITCH ant the two agents Franz and Louis with input F_1, L_1 and output F_2, L_2 is given by

$$\left|W_{\text{switch}}\right.^{+} := |F \to L\rangle \otimes |0\rangle^{\mathcal{F}_C}\rangle + |L \to F\rangle \otimes |1\rangle^{\mathcal{F}_C}, \tag{2.5}$$

where $|0\rangle^{\mathcal{F}_C}$, $|1\rangle^{\mathcal{F}_C}$ are the Choi-vectors of the future control qubit and $|F \to L\rangle$ and $|L \to F\rangle$ are the process vectors, that describe either Franz or Louis acting in past of the other:

$$|F \to L\rangle = |\mathbb{1}\rangle^{\mathcal{P}_T, F_1} \otimes |\mathbb{1}\rangle^{F_2, L_1} \otimes |\mathbb{1}\rangle^{\mathcal{F}_T, L_2} \tag{2.6}$$

$$|L \to F\rangle = |\mathbb{1}\rangle\rangle^{\mathcal{P}_T, L_1} \otimes |\mathbb{1}\rangle\rangle^{L_2, F_1} \otimes |\mathbb{1}\rangle^{\mathcal{F}_T, F_2} \tag{2.7}$$

$|\mathbb{1}\rangle\rangle$ represents the identity Choi-vector $|\mathbb{1}\rangle\rangle = \sum_i |i\rangle \otimes |i\rangle$ that up to a normalisation factor describes a maximal entangled quantum state [17].

2.2.1 The Commutation Game

The so-called "Commutaton Game" was the first experimental test for indefinite causal order [4]. It demonstrates the quantum SWITCH's ability to differentiate between commuting and anticommuting quantum gates in a single run through the setup, outperforming any classical quantum circuit that requires at least two runs.
Considering two observables A and B as well as two operators $\hat{A}$ and $\hat{B}$ with a shared eigenfunction ψ_0, which means that:

$$\hat{A}\psi_0 = a\psi_0 \tag{2.8}$$

$$\hat{B}\psi_0 = b\psi_0 \tag{2.9}$$

Measuring A and B of a physical system in state $|\psi_0\rangle$ will thereby result in a, or b if it fulfils:

$$ab\,|\psi_o\rangle - ba\,|\psi_0\rangle = \hat{A}\hat{B}\,|\psi_0\rangle - \hat{B}\hat{A}\,|\psi_0\rangle = [\hat{A}, \hat{B}]\,|\psi_0\rangle = 0 \tag{2.10}$$

Which will always be satisfied if:

$$[\hat{A}, \hat{B}] = 0 \tag{2.11}$$

If $\hat{A}$ and $\hat{B}$ satisfy (2.11) we say that these two operators commute. We refer to operators as anticommuting when the following relation holds:

$$ab\,|\psi_o\rangle + ba\,|\psi_0\rangle = \hat{A}\hat{B}\,|\psi_0\rangle + \hat{B}\hat{A}\,|\psi_0\rangle = \{\hat{A}, \hat{B}\}\,|\psi_0\rangle = 0 \tag{2.12}$$

resulting in:

$$\{\hat{A}, \hat{B}\} = 0 \tag{2.13}$$

In quantum mechanics, commuting operators have a unique significance. Their commutation indicates that measurement outcomes do not depend on the order of operations. Additionally, it allows for the simultaneous measurement of corresponding observables with arbitrary precision, unaffected by the Heisenberg uncertainty principle.
In the commutation game, the participants receive two unitary gates, U_1 and U_2 and they are told that these gates either commute or anticommute. To win the the game they must determine which statement is true, but you can only use each gate once.
For a classical circuit, two runs are required to test whether two operators commute or anticommute, as the order must be swapped at least once so that the results can be compared.
However, as demonstrated by Procopio et al. [4], one only requires a single use of each gate when using a quantum Switch that can utilise the superposition of orders. The test requires two unitary gates U_1 and U_2 of which is only known that they either commute or anticommute. With a control-qubit in the state $|+\rangle_C = \frac{1}{\sqrt{2}}\big(\ |0\rangle_C + |1\rangle_C\big)$ and an arbitrary target qubit $|\psi\rangle_T$, the state that enters the quantum SWITCH is:

$$\frac{1}{\sqrt{2}}\big(\ |0\rangle_C + |1\rangle_C\big)\,|\psi\rangle_T \tag{2.14}$$

For the control qubit in $|0\rangle_C$, the target qubit will see the unitary gates in the order U_2, U_1, while the control qubit in $|1\rangle_C$ it will pass through the system in the order U_1, U_2. Right after the SWITCH a Hadamard gate is applied to the control qubit, this results in an output state:

$$\frac{1}{2}\,|0\rangle_C\,\{U_1, U_2\}\,|\psi\rangle_T + \frac{1}{2}\,|1\rangle_C\,[U_1, U_2]\,|\psi\rangle_T \tag{2.15}$$

Meaning that we can distinguish commuting from anticommuting operators by measuring the control qubit. Satisfying either equation 2.11 or 2.13, we will measure the control-qubit in $|0\rangle_C$ if U_1, U_2 commute, or in $|1\rangle_C$ if they anticommute.

2.3 The Local Causal Inequality

The following description follows the content of van der Lught et al.'s paper "*Device-Independent Certification of Indefinite Causal Order in the Quantum Switch*" [1].

It has been shown, that a quantum SWITCH, as a representative of the class of quantum circuits with quantum control of causal order, can not break any of the causal inequalities that had been described in the past [10]. However a recent study by van der Lught et al. [18] was able to prove, that the quantum SWITCH is able to demonstrate a different device independent certification of indefinite causal order called a Local Causal Inequality (LCI). Although one can choose different constrains, those chosen for van der Lugts version of the local causal inequality are taken from spatiotemporal information and Relativistic Causality assumption to rule out influences outside the future lightcone. Thus, assuming no superluminal or retrocausal influences and given a space-like separated observer, a device-independent certification of an indefinite causal process in a quantum SWITCH

becomes possible [1].
In order to fulfil these constraints the process between two parties, described in 2.1 gets extended by two more agents: A space like separated agent called Bob (B) and a time like separated agent called Charlie (C). For consistency with the paper by van der Lught et al., the two parties whose temporal order is in question are renamed to Alice1 ($A1$) and Alice2 ($A2$) and will be placed inside the quantum SWITCH. Each party is allowed to choose their settings (x_1, x_2, y, z) and take measurements (a_1, a_2, b, c).

The LCI is relying on three assumptions: Definite causal order, relativistic causality and free intervention.
The assumption of a definite causal order is introduced by a hidden variable $\lambda \in \{1, 2\}$, which dictates the partial order. For $\lambda = 1$, the order is $A_1 \prec_1 A_2 \prec_1 C$, while for $\lambda = 2$, it becomes $A_2 \prec_2 A_1 \prec_2 C$. In the first case, Alice2 cannot signal to Alice1; in the second, the restriction is reversed. In both cases, Charlie cannot signal to anyone. Thus, the existence of such a hidden variable would rule out the possibility of an indefinite causal order.
Via the assumption of relativistic causality, it is ensured, that the causal order $\prec_\lambda$ respects the space-time structure of the experiment. This assumption is established by positioning Bob so that he is space-like separated from A_1, A_2, and C, making him $\prec_\lambda$-independent of these events. Retrocausation is ruled out by placing Charlie in the future light cone of Alice1 and Alice2. Thus, for any λ, the conditions $C \nprec A_1$ and $C \nprec A_2$ are met.
Finally the assumption of free intervention is realised by ensuring that the settings x_1, x_2, y, z are independent of any relevant causal influences. This implies that a propability distribution $p(a_2 a_2 bc \mid x_1 x_2 yz) =: p(\vec{a}bc \mid \vec{x}yz)$ can be written as

$$p(\vec{a}bc \mid \vec{x}yz) = \sum_{\lambda \in \{1,2\}} p(\lambda) p(\vec{a}bc \mid \vec{x}yz\lambda) \tag{2.16}$$

Crucially, the settings are statistically independent of λ and, for any value of λ, cannot be influenced by any measurement results outside their $\prec_\lambda$-future.
With $\perp\!\!\!\perp_q$ symbolising statistical independence, one can shorten statistical relation terms like $\forall \vec{a}, c, \vec{x}, y, y', z : \sum_b q(\vec{a}bc \mid \vec{x}yz) = \sum_b q(\vec{a}bc \mid \vec{x}y'z)$ to the simpler expression $\vec{a}c \perp\!\!\!\perp_q y$. Thus, the no-signalling conditions above can be formulated as $p(\cdot \mid \cdot\lambda) \in \mathcal{DRF}$, including the set of probability distributions $\mathcal{P}_{\vec{a}bc|\vec{x}yz}$:

$$\mathcal{NS} := \{q \in \mathcal{P}_{\vec{a}bc|\vec{x}yz} : \vec{a}c \perp\!\!\!\perp_q y \text{ and } b \perp\!\!\!\perp_q \vec{x}z\} \tag{2.17}$$

$$\mathcal{DRF}_1 := \{q \in \mathcal{NS} : a_1 b \perp\!\!\!\perp_q x_2 \text{ and } \vec{a}b \perp\!\!\!\perp_q z\}\,; \tag{2.18}$$

$$\mathcal{DRF}_2 := \{q \in \mathcal{NS} : a_2 b \perp\!\!\!\perp_q x_1 \text{ and } \vec{a}b \perp\!\!\!\perp_q z\} \tag{2.19}$$

Where $\mathcal{NS}$ represents the set of correlations with no signalling between Bob and all other agents. This is fulfilled if the outcomes of Alice and Charlie are independent of Bob's setting ($\vec{a}c \perp\!\!\!\perp_q y$), and in turn, Bob's result is independent of all other settings ($\vec{a}b \perp\!\!\!\perp_q z$).

$\mathcal{DRF}_1$ and $\mathcal{DRF}_2$ are subsets of these correlations that satisfy the assumptions of Definite Causal Order ($\mathcal{D}$), Relativistic Causality ($\mathcal{R}$), and Free Interventions ($\mathcal{F}$).
$\mathcal{DRF}_1$ contains all probability distributions from $\mathcal{NS}$ that additionally ensure that Alice-1's and Bob's outcomes are independent of Alice-2's setting ($a_1 b \perp\!\!\!\perp_q x_2$), which is always the case if Alice-1 is in the causal past of Alice-2 and by Bob's space-like separation. That the outcomes of all other parties are independent of Charlie's setting ($\vec{a}b \perp\!\!\!\perp_q z$), which is fulfilled when Charlie acts in the causal future of all other agents.
$\mathcal{DRF}_2$ is the subset of $\mathcal{NS}$ that similarly includes the time-like separation of Charlie but is combined with the condition that Alice-2 is in the causal past of Alice-1, such that a_2 cannot be influenced by x_1, and again, Bob's outcome remains independent due to his space-like separation.
Together, $\mathcal{DRF}_1$ and $\mathcal{DRF}_2$ represent those probability distributions that can be considered for the construction of a LCI.
In particular, limiting all variables $a_1, a_2, b, c, x_1, x_2, y, z$ to take values only in $\{0, 1\}$, assuming that the settings x_1, x_2, y, z are uniformly distributed and they obey the above restrictions of $\mathcal{DRF}$ the local causal inequality can be expressed as

$$\underbrace{p\,(b=0, a_2=x_1 \mid y=0)}_{\text{(I)}} + \underbrace{p\,(b=1, a_1=x_2 \mid y=0)}_{\text{(II)}} + \underbrace{p\,(b \oplus c = yz \mid x_1=x_2=0)}_{\text{(III)}} \leqslant \frac{7}{4} \tag{2.20}$$

With $\oplus$ as addition modulo 2, it acts on the measurement results b, c such that for $(b=c=1)$ or $(b=c=0)$, $b \oplus c = 0$, and for $(b=0,\ c=1)$ or $(b=1,\ c=0)$, $b \oplus c = 1$. This inequality satisfies the conditions of parameter independence (PI) and measurement independence (MI) (also known as free choice) through relativistic causality and free interventions. Every hidden variable model that meets these conditions, where only one of the measurement outcomes of one party is linked to the hidden variable λ, satisfies the Clauser-Horne-Shimony-Holt (CHSH) inequality. Due to the free choice condition, any influence of λ on the settings x_1 and x_2 is prohibited. Therefore, assuming a hidden causal variable λ exists and that the first two terms sum to 1, this hidden variable is correlated with Bob's measurement result. Consequently, Charlie and Bob are unable to violate the CHSH inequality represented in the third term, meaning it cannot exceed $\frac{3}{4}$.
To illustrate how the quantum SWITCH can violate this LCI, let's consider a two-photon Bell state $|\Phi^+\rangle_{C,B} = \frac{1}{\sqrt{2}}(|H\rangle_C |H\rangle_B + |V\rangle_C |V\rangle_B)$, shared by Bob and the other space-like separated parties, where it serves as a control qubit for the quantum SWITCH.
Bob measures in the computational basis if $y=0$ or in the diagonal basis if $y=1$, and he records the outcome b. Alice1 and Alice2 operate within the SWITCH, while Charlie acts outside the SWITCH in their temporal future.
Additionally, a target qubit is prepared in $|H\rangle_T$ and sent into the quantum SWITCH. Upon receiving the photon, both Alices always measure the target qubit in the computational basis for any value of x_1 and x_2 and obtain their outcomes a_1 and a_2. They then prepare the target as $|x_1\rangle_T$ and $|x_2\rangle_T$, respectively. Afterwards, the photon reaches Charlie, who measures only the control qubit. For the setting $z=0$, Charlie measures the state in the $X+Z$ direction; for $z=1$, he measures in the $X-Z$ direction, resulting in the outcome

c.
The first term **(I)** of inequality 2.20 describes the probability that Bob measures $b = 0$ in the computational basis when $y = 0$. This result projects the control qubit to $|0\rangle c$, placing Alice-1 in the causal past of Alice-2, such that Alice-2 receives Alice-1's setting. Hence, her measurement result is determined by this setting, $a_2 = x_1$. Since Bob measures one part of the Bell state $|\Phi^+\rangle$, the polarisation appears to him as a completely mixed single-qubit state, $|\psi\rangle mix = \frac{1}{2}(|H\rangle\langle H| + |V\rangle\langle V|)$. This implies that the probability of him measuring $b = 0$ is $\frac{1}{2}$.
(II) refers to the probability of a similar situation, only this time Bob's result is $b = 1$, which sets the SWITCH in the configuration where Alice-2 operates in Alice-1's causal past, meaning that $a_1 = x_2$. Again, the probability for $b = 1$ equals $\frac{1}{2}$. Thus, **(I)** and **(II)** sum up to 1.
(III) is the CHSH term that relies on the entanglement between Charlie's and Bob's qubits. The condition $x_1 = x_2 = 0$ ensures that the settings in the SWITCH form an identity operation. $b \oplus c = yz$ defines the relation between Bob's and Charlie's settings and measurements. For example, if $yz = 0$, the results b, c must be equal so that $b \oplus c = 0$. Bob measures in the computational basis and has a probability of $\frac{1}{2}$ to get the output $b = 0$. With $z = 1$, Charlie has to measure in the $(Z + X)$ basis (see appendix (A)):

$$\begin{aligned}
|0\rangle_{Z+X} &= \frac{1}{2}\left(\sqrt{2+\sqrt{2}}\,|H\rangle + \sqrt{2-\sqrt{2}}\,|V\rangle\right), \\
|1\rangle_{Z+X} &= \frac{1}{2}\left(-\sqrt{2-\sqrt{2}}\,|H\rangle + \sqrt{2+\sqrt{2}}\,|V\rangle\right),
\end{aligned} \tag{2.21}$$

Since Charlie and Bob share a $|\Phi^+\rangle$ Bellstate Bobs measurement projects Charlie's qubit to $|0\rangle$. This rises Charlie's chance to obtain $c = 0$:

$$P(z = 0)) = Tr(|H\rangle\langle H|\,(|0\rangle\langle 0|)_{Z+X}) = \frac{1}{2} + \frac{\sqrt{2}}{4}. \tag{2.22}$$

With this $CHSH$-value of $\frac{1}{2} + \frac{\sqrt{2}}{4}$ the local causal inequality 2.20 is broken by

$$\underbrace{\frac{1}{2}}_{\text{(I)}} + \underbrace{\frac{1}{2}}_{\text{(II)}} + \underbrace{\frac{1}{2} + \frac{\sqrt{2}}{4}}_{\text{(III)}} \approx 1.8536 > \frac{7}{4} \tag{2.23}$$

This result is the maximum violation that can be reached with the local causal inequality and indicates that, under the assumptions of relativistic causality and free interventions, an indefinite causal order emerges in the quantum SWITCH that that defies explanation by a hidden variable.

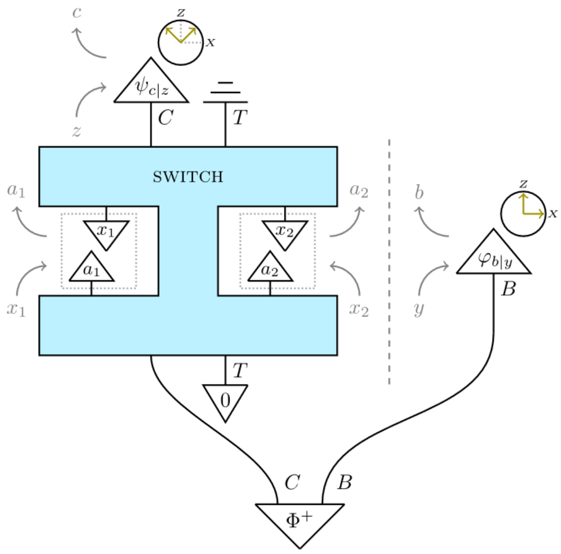

Figure 2.3: **Overview of the arrangement to break the LCI timeline running from the bottom to the top:** The Bell state $|\Phi^+\rangle_{C,B} = \frac{1}{\sqrt{2}}(|H\rangle_C |H\rangle_B + |V\rangle_C |V\rangle_B)$ is shared between the space-like-separated agent Bob (B) and the quantum SWITCH. Bob operates on his qubit $|\varphi\rangle$ with settings y and outcomes b. Additionally, the target qubit $|0\rangle_T$ is sent into the SWITCH. The settings and measurements of Alice1 and Alice2 (a_1, a_2, x_1, x_2) are represented in the process matrix diagram. After the SWITCH, the target qubit is discarded, and Charlie (C) measures the control qubit $|\psi\rangle$ with setting z and outcome c. Adapted from Van Der Lugt et al., Nature Communications 14, 5811, p. 4.[1]

If Alice1 and Alice2 do not manipulate the target state or reprepare it in $|0\rangle_T$, the conditions $a_2 = x_1$ from term I and $a_1 = x_2$ from term I in eq.2.20 are always fulfilled, independently from the causal order and the process resembles a standard Bell test. This would also be the case if Bob manipulates his measurement via post selection to set the control-qubit to exclusively $|0\rangle_C$ and thereby defining the temporal order of Alice1 and Alice2.

3 | Methods

In this section of the thesis, both the experimental setup and the measurement methods employed will be described. Initially, an overview of the entire experimental arrangement will be presented. Following this, the critical components will be examined in detail, including a description of their functionality.

3.1 Setup and Functionality of the Experiment

The photons for this experiment are generated in a down-conversion single-photon source, which is described in detail in section3.2. For clarity, the two photons that form a two-photon state will be referred to as "signal" and "idler." The idler photon is sent directly via an SMF-28 single-mode fibre to Bob's tomography stage. Along the fibre path, a section is coiled into a set of polarisation controller paddles. A 60FC-SF-4-M8-08 single-mode fibre collimator with an 8 mm focal length, built by Schäfter+Kirchhoff, couples the photons into the free-space section.
Since this type of collimator has a flexible focus suitable for different wavelengths, ranging from 980 nm to 1550 nm, it must be adjusted to 1550 nm before being positioned in the setup. To achieve this, it is connected to a fibre linked to an alignment laser operating at the same wavelength. Here we always use an EXFO tunable continuous wave (CW) laser for alignment. The beam from the collimator is then tracked using an infrared-sensitive laser viewing card. If the beam appears too wide and diffuse or focuses to a point in front of the collimator, the focus must be adjusted. This is done by carefully fine-tuning the thread at the tip of the collimator. Once the beam appears parallel, the correct focus has been roughly achieved.
After the photon enters Bob's free-space section, it passes through two waveplates mounted on manually adjustable turntables: first a half-wave plate (HWP), followed by a quarter-wave plate (QWP) fixed at 45° relative to the fast axis. Together with the polarisation controller, these waveplates are used for polarisation compensation, as described in section 3.4.2.
Afterwards, the photon enters the actual tomography stage. First, it passes through a QWP, then through a HWP, and finally through a polarising beam splitter (PBS). These waveplates are mounted on motorised rotation mounts. All of the motorised mounts in this setup are the ELL14K type by Thorlabs, equipped with resonant piezoelectric motors. They are controlled via an interface board and an additional bus distributor, allowing multiple motors to be connected to a single USB port.
Depending on whether the photon is reflected or transmitted by the PBS, it is directed by two mirrors in each path into one of two fibre collimators. These collimators are of the same type as the one used at the beginning to couple photons from the fibre into the

free-space section.
As the preliminary focus adjustment of the collimators is not optimal, it must be fine-tuned during the coupling process to maximise coupling efficiency. Both output collimators are connected to SMF-28 single-mode fibres, which guide the photons to the two-channel fibre input for further transmission to the superconducting nanowire single-photon detector (SNSPD)s in a cryogenic system built by Photonspot Inc. Since the detection efficiency of SNSPDs is influenced by photon polarisation, each fibre leading to the detectors is equipped with a fibre paddle polarisation controller.
When a photon is detected in a SNSPD it creates an electric pulse that is then amplified by in an external amplifier box so that the electric signals are high enough to be processed by a time tagger. We use here a "Time Tagger Ultra" produced by Swabian instruments with a RMS-jitter of 8 ps [19].
If a photon is detected in the SNSPD connected to Bob's H-path, the electrical signal is split immediately after the amplifier by a BNC T-piece, so that the signal not only reaches the tagger but is also sent to a discriminator, which generates a rectangular pulse from each photon signal. These pulses are then sent to trigger two signal generators. With an appropriate delay, these generators will trigger optical switches in the signal setup.
For the measurement of the local causal inequality, it is planned to trigger the signal generators with pulses from the detection of photons from both of Bob's detectors. For the computation game, this is not necessary, as the idler photon is always measured in the diagonal basis to prepare the signal photon in the $|+\rangle$ state. This is achieved by rotating the motorised QWP to 45° and the motorised HWP to −22.5° with respect to their fast axis. Thus, the diagonally polarised photon always ends up in the transmitted path of the PBS. (A more detailed description of this method can be found in section 3.5.2).
Before the signal photon reaches the input coupler of the free-space section, it must travel through a 1 m long delay fibre to compensate for the time needed for the trigger signal to reach the signal generators. From there, it passes through a fibre circulator and enters the free-space section of the time-bin interferometer. A circulator is a fibre-optical device with three inputs/outputs that allows photons to travel in only one direction, exiting at the next output. In this case, the photon enters through input #1 and therefore exits at output #2 towards the interferometer. There a PBS splits the path into a long and a short arm. Depending on the polarisation, the photon will travel along one of these paths or both in a superposition. In this way, the polarisation qubit is converted into a time-bin qubit (this process is described in detail in section 3.3).
At this point, after the photon has passed the first optical switch (to prevent confusion with the other optical switches, this will be called time-bin switch), both time bins have horizontal polarisation and form the control qubit for the quantum SWITCH. The photon then enters the so-called target-qubit preparation section. For all experiments described in this thesis, this section only contains a PBS that ensures no other than horizontal polarisation $|H\rangle_T$ can enter the quantum SWITCH. Since future experiments may involve testing other target-qubit input states, this section can be equipped with additional waveplates.
Since the optical switches do not operate with absolute accuracy and have limited speed,

there might be leakage into the other output. To prevent any photon from entering the quantum SWITCH from the opposite direction, a circulator is placed at this time bin switch's output. Any photon reaching the circulator from this side will be directed to the dead end of circulator exit #3 and discarded.
Once the photon reaches the quantum SWITCH, the optical input switch is triggered so that it is tuned to the parallel configuration when the later (long) time bin $|L\rangle$ arrives. In this way, the first (short) time bin $|S\rangle_c$ passes the switch diagonally and enters Alice-2's section first, while $|L\rangle_c$ encounters Alice-1's section first. For the measurement of the LCI, both sections will be equipped with a polarisation filter to perform a measurement, as well as a HWP to prepare a new state afterwards. For the computation game, these have been replaced by three motorised waveplates in the order QWP, HWP, QWP. Additionally, two pairs of compensation waveplate sets (see 3.4.1) are always positioned in these sections.
The second optical switch must now be synchronised to switch for the $|L\rangle_c$ qubit. This ensures that both qubits exit through the same output and are then directed into the fibre, leading them back to the input of the SWITCH. At this point, they each enter the section they have not yet visited.
If the control qubit is in a superposition of $|S\rangle_c$ and $|L\rangle_c$, the entire process through the quantum SWITCH occurs in a superposition of orders.
On the way back to the interferometer, the photon passes through a short free-space section, installed to allow polarisation compensation for all fibre paths in this direction between the SWITCH and the free-space section of the interferometer. After this, it reaches the circulator mentioned earlier. However, since the photon enters from the opposite direction this time, it exits through #2 and reaches the time-bin switch from the other side. The switch is now triggered again, leading the short time-bin $|S\rangle_c$ into the long interferometer arm and $|L\rangle_c$ into the short arm. This reverses the time difference between the bins, reuniting them at the PBS. Since they now encounter the PBS from different sides, they split according to the polarisation carried by their target qubit at this point.
The previous $|S\rangle_c$ part enters the PBS in such a way that its horizontally polarised component is transmitted into Charlie-0's tomography stage, while its vertically polarised part is reflected back into the former input path of the interferometer. From there, it re-enters the single-mode fibre, and upon reaching the circulator, it is directed into Charlie-1's tomography section.
The former $|L\rangle_c$ qubit, on the other hand, now reaches the PBS from the short interferometer arm. Its horizontal component is transmitted into the fibre path towards Charlie-1's tomography stage, while the vertical polarisation is reflected into Charlie-0's setup section. This sorting process allows for the later reconstruction of both the control qubit and the target qubit.

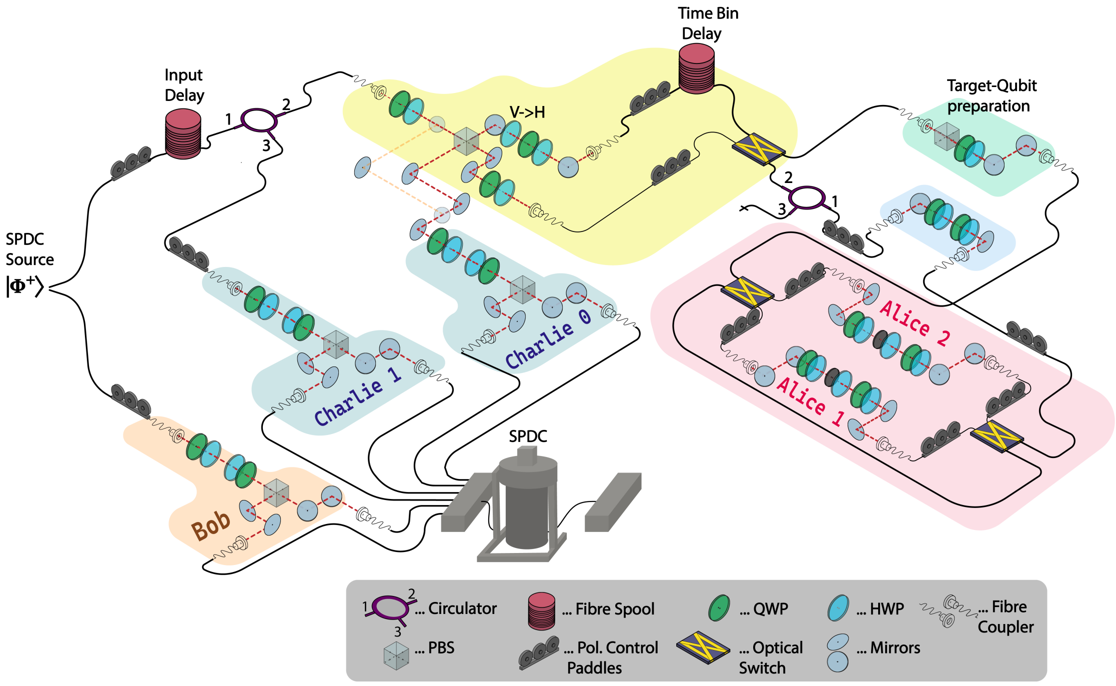

Figure 3.1: **Illustration of the full optical setup:** This shows the setup in the configuration as it will be used for the measurement of the LCI, where a polarisation filter and a HWP are placed in each arm of the quantum SWITCH.

3.1.1 Optical Switch Synchronisation

Once the electrical trigger signal reaches the function generators, they must be configured correctly to trigger the optical switches at the precise moment and with the appropriate pulse settings. This section will describe how to determine the optimal synchronisation settings.
The optical switches used in this setup are of the type "Nanona - Ultra Fast Optical Switch" produced by Boston Applied Technologies Inc., capable of switching at rates up to 1 MHz for wavelengths between $1310 - 1550$ nm. Passively, they remain in the crossed state and switch to parallel when their driver receives a 5 V electrical signal.
Each function generator is equipped with two channels that can output signals with independent settings. Via an optional burst-mode these signals can be timed to a trigger pulse received by the generator.
The time-bin switch must operate for the photons both when they arrive from the interferometer and when they return from the quantum SWITCH. These two events need to be triggered individually. Therefore, both output channels of one signal generator are combined via a BNC T-piece so that both pulses reach the time-bin switch driver.
First, the timing for the input pulse must be determined. To achieve this, an additional single-mode fibre is connected to the third output of the circulator behind the time-bin switch, which usually serves as a dead end. The other end of the fibre is connected to the

input of an SNSPD detector. The histogram between this detector and the one measuring Bob's triggering photon is then measured in an ongoing loop.
The signal generator is set to burst mode, and the first channel is configured to generate a rectangular signal with a total duration of 130 ns and a duty cycle of 86%, which corresponds to the proportion of time the signal remains at the high level. The high level is initially set to 5 V, while the low level is fixed at 0 V.
Now the time delay for the generated signal must be found. Initially, it is set to 0 ns, which means that the signal generator immediately sends out the signal when the trigger pulse arrives. Since this is most likely too early, the switch does not switch for the $|L\rangle_c$ photon, which thereby ends up in the circulator output. This means that the histogram will display a high peak at the time difference between the signal and idler. Now the time delay is slowly increased. When the switch is triggered closer to the arrival time of $|L\rangle_c$, this peak will shrink until it nearly disappears. This is then the optimal delay for the first pulse for the time bin switch.
For the optical switches used in the quantum SWITCH, the signal generator is configured to produce a sequence of two signals, each with a length of 300 ns and a duty cycle of 42%. Initially, the high level is set to 5 V.
Next, the appropriate delay must be found for the input switch of the quantum SWITCH. Here, it needs to be triggered at the arrival time of the $|L\rangle_c$ qubit, which is intended to reach Alice-1's setup first. To do this, the single-mode fibre is moved from the circulator exit to the switch exit towards Alice-2. If the input switch is not triggered, both time bins will arrive there and appear in the histogram. If it is triggered with no time delay, the switch might activate when $|S\rangle_c$ arrives, resulting in only $|L\rangle_c$ being shown in the histogram. If the time bins have not been observed together before, this peak could be mistaken for the short time bin.
Now, the delay time is gradually increased until the peak of the later time bin reaches its minimum and the $|S\rangle_c$ peak is maximised. Once this is achieved, the high level of the generated pulse can be adjusted to find the setting that yields the best result. Although this should theoretically be at 5 V, some of the optical switches appear to operate more precisely at lower voltages.
To synchronise the output switch, the detector fibre is connected to the fibre that leads out of the switch towards the polarisation compensation section. This quantum SWITCH was originally built by Michael Antesberger for the measurement of a process matrix [17]. It was designed so that the time delays of the input and output switches are identical, allowing the photon to pass through the optical switches in the correct order. However, since the setup has undergone several changes, including the replacement of some of the optical switches, this condition is no longer completely fulfilled. Perhaps due to different lengths of the BNC cables or other variations in the electronics, the signal for the output switch must now be sent slightly earlier than the input signal.
Once the correct delay is established, the photons pass through each optical switch twice before reaching the detector fibre. If the delay of the output switch is set too early, it is possible for the photon to leave the SWITCH after visiting only one of the Alices. Without careful attention to the timing of the peaks, this may appear identical in the

histogram. Additionally, due to leakage, there will always be two earlier peaks in the histogram that can appear larger than the correct ones if the switch does not operate as intended or if some of the photons disappear during the journey between the first and second passes(e.g., due to a broken fibre or a poor choice of the Voltage). A quick method to distinguish between these two pairs is to block the path in either Alice-1's or Alice-2's section. In the case of leakage, this will result in the disappearance of one of the peaks, while both of the correct peaks will vanish.
Finally, the last delay must be determined for the time-bin switch. The procedure is the same as for the first signal, except that it is not necessary to start the search at 0 ns. Considering the time required for the photons to travel through the setup, it is sensible to begin with a minimum delay of 500 ns. Once this timing is correctly set, the appropriate high-level voltages must be identified for both signal generator channels that trigger the time-bin switch. Since the signals are combined into one BNC cable, they may influence each other, which can interfere with the performance of this optical switch. It has been found that the input switching will be compromised by the second pulse if the first one is not set close to 5 V, even though a lower voltage had yielded good results before the second pulse was added.

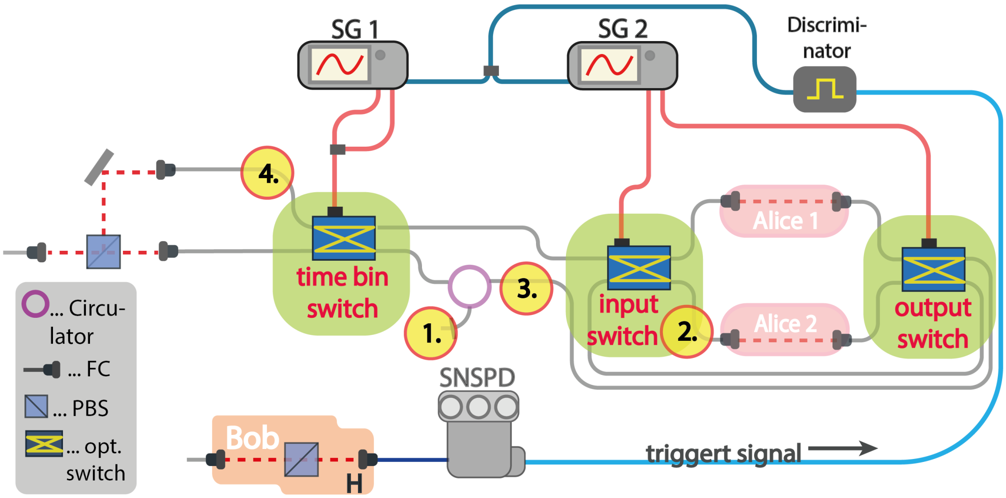

Figure 3.2: **Sketch to illustrate the optical switch synchronisation process:** The electrical trigger signal is initiated by a detection event in Bob's detector from the H-path. This signal is converted into a rectangular pulse by the discriminator, which is then sent to the signal generators SG1 and SG2. SG2 generates the trigger pulses for the quantum SWITCH, while SG1 triggers the time-bin switch from both channels. The numbered circles (1-4) indicate the positions where the detector fiber is connected during the process of determining the correct time delays for each generated signal.

3.1.2 Optimising the PBS Extinction Ratio

It turned out that the PBS used in most parts of this setup are highly sensitive to the angle of the incoming beam. Therefore, it is necessary to find the optimal position before aligning the subsequent paths. This is achieved by sending the beam of the alignment laser through the setup into the PBS. A polarisation filter set to HH and a HWP are placed directly in front of the PBS, with a power meter positioned as close as possible behind the reflected output.
First, the HWP is rotated so that the power reaches a minimum. Then, the PBS is carefully rotated to adjust the input angle. To ensure that this rotation is parallel to the optical table, the PBS is fixed directly to a metal post in a post holder and secured at a specific height using a clamp. During this rotation, the power will either rise or fall depending on the specific angle. The optimal position is indicated by the lowest output power when the PBS is not rotated. too far out of the beam. When the PBS is turned in the correct direction, one will initially observe a decrease in power, which will begin to rise again after a certain point. This minimum position is likely the correct setting. If the power continues to decrease further, it is probably due to beam displacement and not indicative of a good extinction ratio. In such a case, it is advisable to try rotating in the opposite direction.

Once this minimum is found, the HWP is rotated to the position where the maximum power is reflected. This value should be close to the input power to the PBS. If this is not the case, the found position is not optimal, and the procedure must be repeated. If the the ratio between the highest and lowest power at the reflected output is satisfying, the position must be fixated. Then the ratio at the transmitted path is measured without touching the PBS. The extinction ratio of one port is given by [20]

$$r_e = \frac{P_0}{P_1}. \tag{3.1}$$

One output usually shows a better result than the other; however, the extinction ratio of both PBS outputs should not be far above 0.001.

3.2 Type-0 down conversion single photon source

The single-photon pairs for this experiment are generated by a bright Type-0 spontaneous parametric down-conversion (SPDC) source, that has previously been described by Neumann et al. in their paper *"Experimental Entanglement Generation for Quantum Key Distribution beyond 1 Gbit/s"* [21]. After being transported to our laboratory, the source required some adjustments to function as intended. This section first outlines working principle of the source and then describes the setup specific setup, that has been used in this experiment.

3.2.1 Characteristics of a type-0 SPDC source

Boiled down to the essentials, SPDC refers to the process in which one photon (from the pump beam, p) is converted into two lower-energy photons (called signal (s) and idler (i)), with energy and momentum conservation governing their respective wavelengths and wave vectors. The energy conservation condition is given by the associated frequencies ω

$$\omega_p = \omega_s + \omega_i. \tag{3.2}$$

The momentum conservation condition results in the wave vector ($\vec{k}$) relation

$$\vec{k}_p = \vec{k}_s + \vec{k}_i. \tag{3.3}$$

Even though this process is often referred to as the reverse process of second harmonic generation (SHG), this can only be considered an intuitive picture of SPDC [22, p. 167], but it is actually incorrect. SHG can be perfectly described by classical electromagnetism, while SPDC requires quantum mechanics, as the conversion from one photon into a photon pair relies on the consideration of vacuum states with no representation in classical physics [23].
To create single-photon states via a SPDC source, a coherent pump beam must be sent into a crystal with second-order susceptibility $\chi^{(2)}$. With a correctly oriented beam and sufficiently strong pump energy, two photons can be generated with polarization states that depend on the type of SPDC process [22, p. 163].
Since the wave vector $\vec{k}$ with amplitude $\left|\vec{k}\right| = \frac{n\omega}{c} = \frac{2\pi n}{\lambda}$ depends of the frequency and simultaneously on the wavelength, the energy and momentum conservation conditions can not be treated independently and are restricted by the refractive index n. To meet all requirements up to tolerable small derivation is called phase matching. For perfect phase matching conditions the phase mismatch equals zero [24]

$$\Delta k = 2\pi \left(\frac{n(\omega_p)}{\lambda_p} - \frac{n(\omega_s)}{\lambda_s} - \frac{n(\omega_i)}{\lambda_i} \right) = 0. \tag{3.4}$$

With the reflective index depending on the respective frequency.Ideal phase matching is archived when

$$\frac{n(\omega_p)}{\lambda_p} = \frac{n(\omega_s)}{\lambda_s} + \frac{n(\omega_i)}{\lambda_i} \tag{3.5}$$

In the case of a degenerated SPDC process, that is given if (i) $\omega_i = \omega_s$ and therefor (ii) $\lambda_i = \lambda_s$, this can be simplified:

$$\begin{aligned} \frac{n(\omega)}{\lambda/2} &= \frac{n(\omega/2)}{\lambda} + \frac{n(\omega/2)}{\lambda} \\ \Rightarrow \quad \frac{2n(\omega)}{\lambda} &= \frac{2n(\omega/2)}{\lambda} \end{aligned} \tag{3.6}$$

$$\Rightarrow \quad n(\omega) = n(\omega/2) \tag{3.7}$$

This can be satisfied by a birefringent crystal that provides different refractive indices depending of the propagation direction and polarisation .
Let's consider a photon travelling in the direction $\vec{k}$ through such a nonlinear crystal with optical axis $\vec{z}$. If the photon's polarisation is oriented orthogonal to the $\vec{k}\vec{z}$-plane, it is referred to as "ordinary" (o); whereas, if the polarisation lies within the plane, it is "extraordinary" (e)-polarised. In general, the generated wave vectors cannot lie in the $\vec{z}$-plane [24].
Depending on the polarisation orientation of the pump and output photons, SPDC is divided into three types [22, p. 128]:

- **Type-0:** ($o \; \rightarrow oo$) or ($e \; \rightarrow ee$)
  In this type, all photon polarisations are either ordinary or extraordinary with respect to the $\vec{k}\vec{z}$-plane.
- **Type-1:** ($e \; \rightarrow oo$) or ($o \; \rightarrow ee$)
  Here, either the pump (p) or the signal and idler (s, i) photons are polarised orthogonal to the $\vec{k}\vec{z}$-plane. The polarisation of the pump is always orthogonal to the polarisation of the signal and idler photons, which share the same polarisation.
- **Type-2:** ($e \; \rightarrow oe$) or ($e \; \rightarrow eo$)
  Here, the pump photon can be either extraordinary or ordinary polarised. The generated signal and idler photons are polarised orthogonal to each other, with one in e-polarisation and the other in o-polarisation.

Which processes are possible in a crystal depends on the specific material. For example in a positive uniaxial crystal the refractive index for extraordinary polarised waves is higher than for ordinary $n_e > n_o$, this results in higher magnitudes of the wave vectors $\vec{k_e}$. For negative uniaxial crystals these relations are just the opposite [24, pp. 131–133] . The SPDC source used in this experiment is of type-0. With all photons in the same polarisation this process is hardly possible via birefringence phase matching. Yet with a periodically polarised crystal it can be realised threw quasi phase matching which will be described in detail later in this section 3.2.1.

The SPDC Hamiltonian

The Hamiltonian $\mathcal{H}$ of the SPDC process is given by the Hamiltonian of the free electric field $\mathcal{H}_1$ and the interacting fields $\mathcal{H}_2$.

$$\mathcal{H} = \mathcal{H}_1 + \mathcal{H}_2, \tag{3.8}$$

with

$$\mathcal{H}_1 = \hbar\omega_m \sum_m (\hat{\mathbf{a}}_m^\dagger \hat{\mathbf{a}}_m + \frac{1}{2}), \tag{3.9}$$

$$\mathcal{H}_2 = \kappa\, \hat{\mathbf{a}}_p \hat{\mathbf{a}}_s^\dagger \hat{\mathbf{a}}_i^\dagger + \kappa^* \hat{\mathbf{a}}_p^\dagger \hat{\mathbf{a}}_s \hat{\mathbf{a}}_i \tag{3.10}$$

where $\hat{\mathbf{a}}^\dagger, \hat{\mathbf{a}}$ represent the creation and annihilation operators for the respective photon p, s, i and $\kappa \in \mathbb{C}$ as a parameter for the interaction strength. $\hbar$ is the plank constant and * represents the Hermitian conjuncgate.

The description provided here largely follows [23]. An alternative approach is to start from the Hamiltonian for light-matter interaction, as described in [22].
The interaction process is the primary focus in most SPDC descriptions. Since using the interaction picture $\mathcal{H}$ can be reduced to the interaction Hamiltonian H_1.
The coherent pump field is significantly stronger than the low intensity of the down-conversion interaction, allowing it to be considered unaffected by the process; thus, the pump operators can be simplified to a complex classical constant

$$\hat{\mathbf{a}}_p \to \alpha_p \in \mathbb{C}. \tag{3.11}$$

Thereby the Hamiltonian simplifies to

$$\mathcal{H}_{SPDC} = \kappa\alpha_p \hat{\mathbf{a}}_s^\dagger \hat{\mathbf{a}}_i^\dagger + \kappa^* \alpha_p^* \hat{\mathbf{a}}_s \hat{\mathbf{a}}_i. \tag{3.12}$$

For a type-0 process, the signal and idler photons are emitted in the same polarisation mode ee or oo [22]:

$$\mathcal{H}_{Type0} = \kappa\alpha_p(\hat{\mathbf{a}}_{Hs}^\dagger \hat{\mathbf{a}}_{Hi}^\dagger + \hat{\mathbf{a}}_{Vs}^\dagger \hat{\mathbf{a}}_{Vi}^\dagger) + \kappa^*\alpha_p^*(\hat{\mathbf{a}}_{Hs} \hat{\mathbf{a}}_{Hi} + \hat{\mathbf{a}}_{Vs} \hat{\mathbf{a}}_{Vi}), \tag{3.13}$$

In the interaction picture the resulting photon state is derived from the interaction at a the time t from where it evolves freely [23]:

$$|\Psi\rangle_t = \mathcal{T} \exp\left[\frac{1}{i\hbar}\int_0^t \mathcal{H}(\tau)d\tau\right]|\Psi\rangle_0 \tag{3.14}$$

The Hamiltonian (3.12, 3.13) is time-independent, so the time-ordering operator $\mathcal{T}$ can be neglected. Limited by the total interaction time, pump power, and the nonlinear properties of the crystal, SPDC remains a very weak interaction process. Under these conditions, it is permissible to approximate the state as

$$\begin{aligned} |\Psi\rangle_t &\approx \left[1 + \frac{t}{i\hbar}\mathcal{H}\right]|0\rangle_s |0\rangle_i \\ &= C_0 |0000\rangle_{H_s,H_i,V_s,V_i} + \frac{C_1}{\sqrt{2}}\big(|1100\rangle_{H_s,H_i,V_s,V_i} + |0011\rangle_{H_s,H_i,V_s,V_i}\big), \end{aligned} \tag{3.15}$$

with the vacuum state $|0\rangle$ state, and created single photon $|1\rangle$ with the respective polarisation H or V. Due to the presumed conditions, this state is only valid for $C_1 \ll C_2$, and therefore the signal and idler modes mostly remain in the vacuum state [23, p. 79].

Quasi phase matching

As mentioned above, effective nonlinear wavelength conversion relies on energy and momentum conservation (this applies to both SPDC and SHG). The momentum conservation criterion (3.3) is also referred to as phase matching; insufficient satisfaction of this criterion will result in destructive interference between the mixing waves. Consequently, the photon pair raten in the nonlinear crystal (NLC) is limited.
For uniaxial crystals, which were the first type of manufactured NLC, phase matching is achieved by aligning the optical axis at a specific angle to the pump beam or by adjusting the temperature [24][25]. However, the number of nonlinear processes that can be achieved via birefringent phase matching is limited, and the bright type-0 down conversion process used here would not be possible through it.
However, the phase matching condition that drives this type of SPDC is not a new concept. In 1962, Armstrong et al. [26] demonstrated that a periodically poled nonlinear medium allows effective nonlinear processes without birefringence and can even tolerate a phase mismatch known as quasi phase matching (QPM). Unfortunately, the manufacturing of such materials was not feasible at that time, as the conversion efficiency is strongly affected by any gaps between the periodically poled layers, which would introduce phase shifts.
It was only after the 1990s, when electric-field poling of ferroelectric crystals was developed, that efficient realisation of QPM became possible. When a strong electric field acts upon a ferroelectric material, it can induce a spontaneous flip of the material's polarisation. The periodic polarisation is achieved by applying a periodic conductive contact onto the surface of the crystal. Under these contacts, the electric field is stronger than in the neighbouring areas, and once the field strength exceeds a critical value with opposite polarity (known as the coercive field), these dipole domains become permanently poled with a period of Λ.
Nowadays, QPM is as common as birefringence phase matching, with most crystals made from lithium niobate, lithium tantalate, or potassium titanyl phosphate (KTP) [24, p. 174].

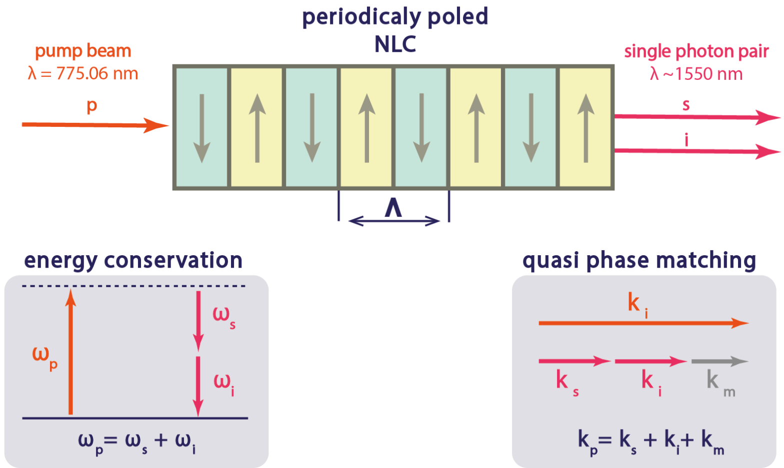

Figure 3.3: **Schematic sketch of a periodically poled crystal:** Each period Λ contains two sections with inverted nonlinear polarisation. The energy conservation condition is perfectly fulfilled by the coherent input pump beam (p) and the generated signal (s) and idler (i) photons, while quasi phase matching (QPM) allows for a phase mismatch of k_m[27][28].

.

For QPM, the constant nonlinear coupling coefficient d_{eff} receives a spatial modulation, which results in a spatially varying coupling coefficient $d(z)$ given by the Fourier series [27]

$$d(z) = d_{\text{eff}} \sum_{m=-\infty}^{\infty} G_m \exp\left(ik_m z\right). \tag{3.16}$$

Here, $G_m = 2\pi m/\Lambda$ represents the magnitude of the grating vector for the mth component of the Fourier series. For a case similar to that described in figure 3.3, the coefficient G_m is

$$G_m = \frac{2}{m\pi} \sin\left(\frac{m\pi}{2}\right) \tag{3.17}$$

and $d(z)$ can be simplified to the square wave-function [27]

$$d(z) = d_{\text{eff}} \;\text{sign}[\cos\left(\frac{2\pi z}{\Lambda}\right)]. \tag{3.18}$$

For the Fourier series (3.16), one term is usually stronger than the others, and the higher-order terms get suppressed. The dominant coupling coefficient d_m depends on G_m (3.17) with $d_m = d_{\text{eff}} G_m$. The desired dominant Fourier term is $m = 1$ [23, p. 95][27]. If this is fulfilled, the phase mismatch Δk_m is given by

$$\Delta k_m = k_s + k_i - k_p - \frac{2\pi}{\Lambda} \tag{3.19}$$

and the coupling coefficient becomes

$$d_m = (2/\pi) d_{\text{eff}}. \tag{3.20}$$

The optimum period for the periodically polarised crystal structure is then given by [27]

$$\Lambda = 2L_{coh} = \frac{2\pi}{k_s + k_i - k_p}, \tag{3.21}$$

with the coherence length L_{coh}.
The interaction between the field and the nonlinear polarisation inside a nonlinear crystal varies. This results in periodic changes in field intensity along the axis of the crystal. It builds up over the length of a coherence length L_{coh} and then decreases for the next length of L_{coh}. The periodic structure in QPM interrupts this pattern, as the reorientation of the medium corrects the phase slip between the generating polarisation and the resulting field. In each section, the sign of the second-order susceptibility $\chi^{(2)}$ is flipped, along with the orientation of the second-order nonlinear polarisation $P^{(2)}$. At the same time, the linear properties remain unchanged due to the inversion of the crystal orientation.
In this way, the intensity can periodically build up along the length of the crystal. The gain per length for QPM does not completely reach the linear gain of perfect phase matching, yet it comes sufficiently close [24, 161 f.].

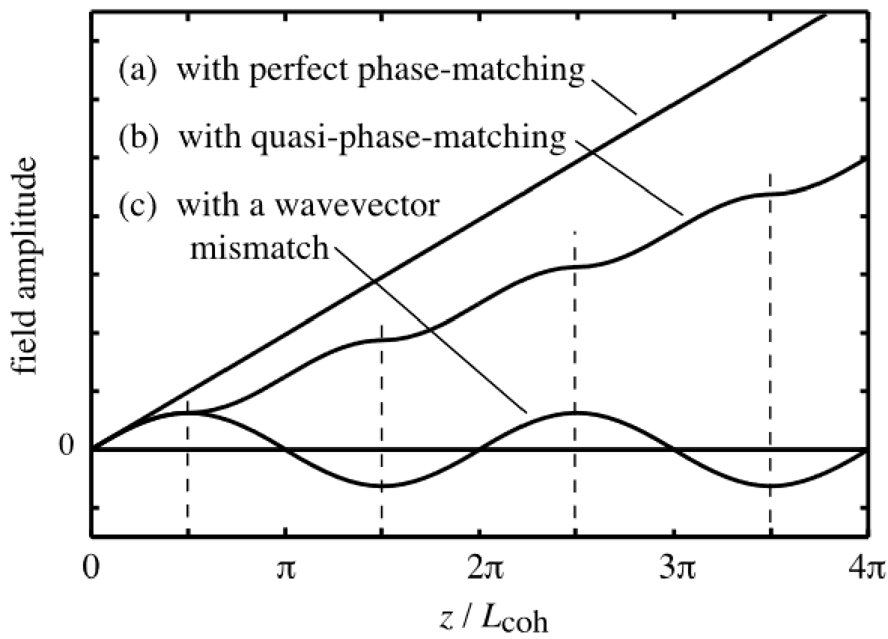

Figure 3.4: **Comparison of the gain for the three phase-matching situations:** (a) With perfect phase matching, the field amplitudes rise linearly with the propagation length inside the crystal. (c) The field gain of quasi-phase matching (QPM) in a crystal with a period of two times the coherence buildup length, $\Lambda = 2L_{coh}$.The amplitude increases over the length of the crystal, albeit with a lower average gradient than in the case of perfect phase matching. (b) For phase mismatch in an uniaxial crystal, the field strength rises and falls periodically. Adapted from [27, p. 81]

3.2.2 The source setup

The SPDC source operates within a Sagnac loop configuration, where the NLC is centrally placed to enable bidirectional pumping (see figure 3.6). The nonlinear, periodically poled 5% magnesium-doped congruent lithium niobate crystal in this source enables type-0 phase matching and bright nonlinear processes. The source is pumped by a CW laser at a wavelength of 775.06 nm. Here, we use a *Toptica TA pro* laser, which allows coarse tuning of the wavelength between 765 nm and 795 nm [29]. While the laser was originally connected to the source via a polarisation maintaining (PM) fiber [21], we have replaced it with a single-mode fiber since the former created fluctuations in the input polarisation mode. Once the coherent pump beam exits the fiber, it meets a PBS, and together with a polarisation controller in the previous fiber section, this setup allows for control of the input power and purification of the pump polarisation.

All vertically (V) polarised light is reflected towards a beam block and discarded, allowing only horizontally (H) polarised light to pass through the PBS. By adjusting the polarisation controller paddles, the amount of H-polarised light is changed, and with it, the number of pump photons reaching the Sagnac loop. After this, the pump polarisation can be manipulated via a HWP. When the fast axis of the HWP is set to either 0° or 45°, the pump polarisation is set to $|H\rangle p$ or $|V\rangle p$, which will later result in a pure yet unentangled two-photon state of either $|VV\rangle s, i$ or $|HH\rangle s, i$. However, when the fast axis is set to $\pm 22.5°$, the pump polarisation becomes $|+/-\rangle p = \frac{1}{\sqrt{2}}(|H\rangle p \pm |V\rangle p)$, and the source will generate a polarisation-entangled Bell state $|\Phi^{\pm}\rangle s, i = \frac{1}{\sqrt{2}}(|VV\rangle s, i \pm |HH\rangle s, i)$ (see results in 4.1).
A focus lens with a focal length of 254 mm focuses the pump beam through a PBS into the NLC. For optimal photon pair creation rates, the size of the Sagnac loop and the focal length of the lens are adjusted relative to each other so that the NLC can be positioned within the Rayleigh length of the pump beam. The loop in this source has a length of 35cm[21]. Depending on the polarisation, the PBS at the entrance directs the path in which the pump beam propagates through the Sagnac loop. With respect to that PBS, we will continue calling the half of the loop straight from the PBS to the crystal the transmitted path (T), and the other half the reflected path (R). Two polarisation filters, set to 0° and 90°, further increase the purity of the polarisation. In R, a dichroic HWP rotated to +45° converts vertical polarisation to horizontal. This allows the NLC to be pumped from both sides with horizontally polarised light, resulting in a wavelength-entangled state with joint polarisation.

$$|V\rangle_p^R \rightarrow \left(\sum_{j=(2k-1)} M_j \left|\lambda_j\right\rangle_s \left|\lambda_{j+1}\right\rangle_i \right) |H\rangle_s |H\rangle_i \,, \tag{3.22}$$

or

$$|H\rangle_p^T \rightarrow \left(\sum_{j=(2k-1)} M_j \left|\lambda_j\right\rangle_s \left|\lambda_{j+1}\right\rangle_i \right) |V\rangle_s |V\rangle_i \,, \tag{3.23}$$

with $j, n \in \mathbb{N}$; $k \in \mathbb{N}_0$ and M_j as a placeholder for a factor related to normalisation and proportion, which depends on the number of generated wavelength pairs and their distribution in the spectrum. Strictly speaking, this should be calculated through integration. However, considering the output as a finite number of discrete pairs, the simplified description using a sum is justified. The The wavelength pairs are restricted by the energy conservation condition $E_p = E_s + E_i$ such that they hold

$$\frac{1}{\lambda_j} + \frac{1}{\lambda_{j+1}} = \frac{1}{\lambda_p} \tag{3.24}$$

.

The photon pair leaves the NLC in a joint direction of either R or L. If the later down-converted pump photon takes the transmitted path through the PBS, the generated photon pair exits the NLC on the opposite side. In this arm of the loop, the polarisation of the pair is then flipped by the HWP. When the pump polarisation is set to either diagonal or antidiagonal $|\pm\rangle_p$, the pump beam propagates through the Sagnac loop in a superposition of the reflected and transmitted arms. With the vertical polarisation rotated to horizontal, the pump photons enter the crystal in the state

$$\frac{1}{\sqrt{2}}(|HT\rangle_p \pm |VR\rangle_p) \rightarrow \frac{1}{\sqrt{2}}(|T\rangle_p \pm |R\rangle_p)\,|H\rangle_p\,. \tag{3.25}$$

Thus, the signal and idler pairs leave the crystal in a superposition of joint directions. The output, immediately after the pair has left the crystal, is the path- and wavelength-entangled state

$$|\phi^\pm\rangle_{i,s} = \frac{1}{\sqrt{2}}(|RR\rangle_{s,i} \pm |TT\rangle_{s,i})\,|\lambda_1\lambda_2 HH\rangle_{s,i}\,. \tag{3.26}$$

As the pair emitted into R experiences a polarisation bit flip, and both paths reunite at the PBS, this results in a polarisation entangled state

$$|\phi^\pm\rangle_{i,s} = \frac{1}{\sqrt{2}}(|VV\rangle_{s,i} \pm |HH\rangle_{s,i})\,|\lambda_1\lambda_2\rangle_{s,i}\,. \tag{3.27}$$

Only a minor part of the pump beam undergoes down-conversion in the crystal, leaving the majority unchanged as it exits the Sagnac loop together with the signal and idler photons through the PBS. From the PBS, both beams exit along the path from which the pump entered the Sagnac loop. There, they encounter a dichroic mirror that is transparent to the 775.06 nm pump photons but reflective to the signal and idler photons at $\sim$ 1550 nm. This separates the generated photons from the pump beam. A collection lens with a focal length of 200 mm [21] focuses the single photons through a long pass (LP) filter into a fibre coupler. This filter absorbs any remaining pump photons. Through a single-mode fibre, the photons are directed into a dense wavelength division multiplexer (DWDM), which divides them by wavelength into different output channels. The source produces an approximately 60 nm broad spectrum of wavelength-entangled photon pairs centred around $\lambda \approx$ 1550.2 nm [21]. The wavelengths of each entangled pair sum up to satisfy the energy conservation condition (3.2). Thus, the signal and idler photons of each pair can be found in individual DWDM channels that satisfy the energy conservation condition 3.24.

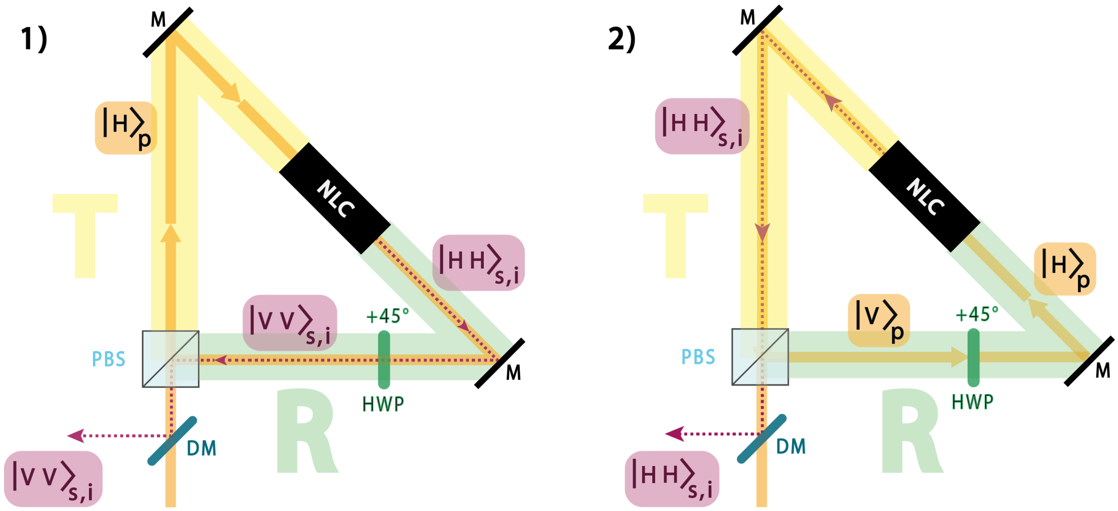

Figure 3.5: **Polarisation of pump beam and generated photons inside the Sagnac loop: 1**) Illustration of how the photon source produces an output state $|VV\rangle s,i$ when pumped with a $|H\rangle p$-polarised beam, despite the type-0 down-conversion process in the crystal: The horizontally polarised pump enters the NLC through the transmitted path (T). Due to phase matching, the signal and idler photons always exit the crystal into the reflected path (R) (with respect to the PBS) in the polarisation state $|HH\rangle s,i$. On their return path, they pass through a dichroic HWP set at 45°, which flips the polarisation to $|VV\rangle s,i$. This allows them to exit the Sagnac loop through the PBS in the correct direction to reach the dichroic mirror (DM). The mirrors (M) in the setup represent classical mirrors that direct the photons around the loop. **2**) If the pump beam is vertically polarised, it is reflected into the R-path at the PBS and passes through the dichroic HWP. Thus, the pump polarisation is set to $|H\rangle p$ when it reaches the crystal, which requires horizontal polarisation for the SPDC. Signal and idler leave the crystal through the T-path in $|HH\rangle s,i$ and can pass straight through the PBS towards the dichroic mirror.

Consequently, several entangled photon pairs could potentially be directed to different locations. For this experiment, the DWDM channels C33 and C35 were chosen, corresponding to a signal photon with a wavelength of $\lambda_1 \approx 1550.92$ nm and an idler photon with $\lambda_2 \approx 1549.32$ nm that with $1/1549.32 + 1/1550.92 \approx 1/775.06$ satisfy the energy conservation condition.
Once the photons have reached the setup, the wavelength difference becomes mostly irrelevant, and only the polarisation entanglement remains important. Since we are pumping the source with $|+\rangle_p$, the resulting two-photon state can therefore be treated as

a polarisation Bell state

$$\left|\Phi^{+}\right\rangle_{s,i} = \frac{1}{\sqrt{2}}(|HH\rangle_{s,i} + |VV\rangle_{s,i}). \tag{3.28}$$

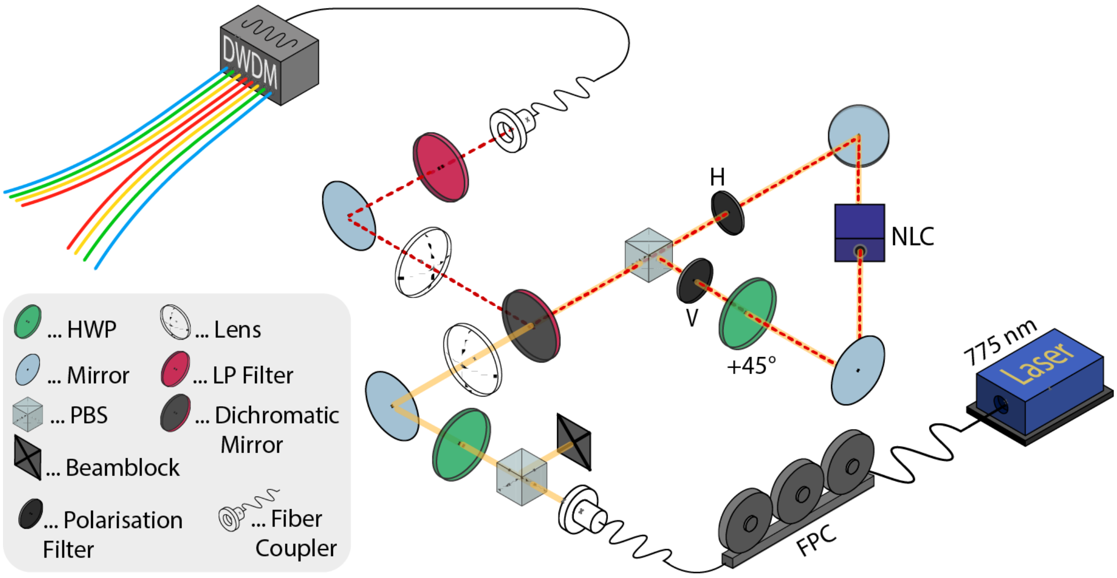

Figure 3.6: **Sketch of the Type-0 SPDC source in a bulk Sagnac configuration:** The source is pumped with a continuous-wave laser at $\lambda = 775.06$ nm, connected via a single-mode fibre to the setup. After leaving the fibre, the pump beam passes through a PBS. This PBS and a polarisation control paddles between the laser and source allow for adjusting the pump power. The discarded part of the beam is blocked, while the transmitted part is purely H-polarised. The pump polarisation is then controlled via a HWP, and a lens focuses the beam into the NLC at the centre of the Sagnac loop. The beam enters the loop through a dichroic PBS, and polarisation filters in both paths enhance purity. A HWP in the reflected path, rotated by 45°, converts V-polarisation to H, enabling the crystal to be pumped with H-polarised light from both directions. The generated photon pair exits the NLC in a joint direction (potentially in superposition) and is recombined at the PBS. With the HWP still in the reflected path, path entanglement can be converted to polarisation entanglement. A dichroic mirror separates the down-converted photons from the pump beam, and a lens focuses the SPDC beam into a fibre coupler. A LP filter removes any remaining pump photons. Finally, the photons reach a DWDM via an SMF-28 single-mode fibre, where they are separated by wavelength and sent to individual destinations. [21].

3.3 Creating time-bin encoded qubits from polarisation

Polarisation qubits are likely one of the most common forms of quantum information in photonic experiments, as they can be easily manipulated using optical elements such as waveplates. However, they are not suitable for all quantum information tasks. In optical fibres, regular adjustments are necessary to correct for polarisation rotations (see section 3.4), and transmission distances are significantly limited by polarisation dispersion [30, pp. 144–147]. Time-bin qubits, on the other hand, utilise the temporal degree of freedom in the photon, are highly stable during fibre transmission, and their detection rate is mainly constrained by detector resolution [31]. Employing time-bin qubits as a control system for the quantum SWITCH provides the significant advantage of passive stability [17]. However, when using a polarisation-entangled SPDC source (3.2), it is necessary to transform the directly produced polarisation qubit into a time-bin qubit. This transformation is achieved by sending the idler photon through an interferometer-like setup, where it passes through a PBS. From there, it will follow one of two paths depending on its polarisation.

For horizontal polarisation $|H\rangle$, the photon travels straight through the PBS and takes the shorter path to the optical switch. For vertical polarisation $|V\rangle$, the photon is reflected within the PBS, passing through a HWP set to 45°. This rotates the polarisation from $|V\rangle$ to $|H\rangle$. The photon then travels through a ~ 308 m long SMF-28 single-mode fibre, resulting in a delay of $\Delta t \approx 151$ ns compared to the photon that took the shorter path. To create time bins from these two paths, they are connected to the two inputs of an optical switch. With the switch in the crossed state, the short time-bin $|S\rangle$ exits through the upper output without further intervention.

However, for the long time-bin $|L\rangle$, the switch must be triggered at the right moment, changing to the parallel state to guide the photon to the same fibre output. This additional step is necessary in this experiment, as we need to reverse the time bins on the way back so they arrive simultaneously at the detectors (see 3.6).

In either approach, the polarisation qubit is transformed into a time-bin qubit in such a way that the superposition is preserved:

$$\alpha |H\rangle + \beta |V\rangle \;\rightarrow\; \alpha |S\rangle + \beta |L\rangle \tag{3.29}$$

Due to the the waveplate in the long path of the interferometer, both time bins have the same polarisation when they leave through the switch. This can be later used as polarisation-target qubit in the quantum SWITCH. With an input polarisation qubit in $|+\rangle$ we receive:

$$\frac{1}{\sqrt{2}}(|H\rangle + |V\rangle)_C \;\rightarrow\; \frac{1}{\sqrt{2}}(|S\rangle + |L\rangle)_C |H\rangle_T \tag{3.30}$$

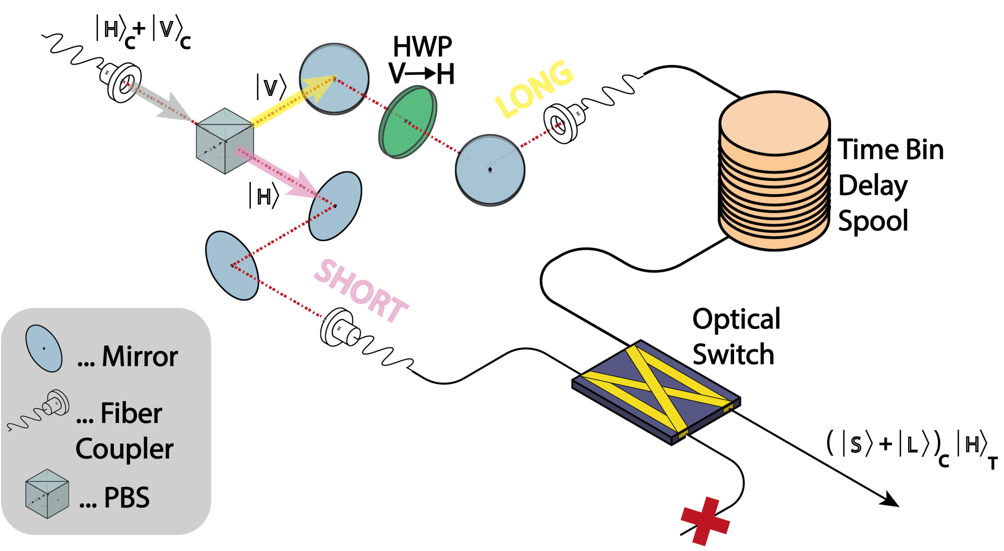

Figure 3.7: **Simplified sketch of the interferometer section:** the signal photon enters the section with the control qubit in a polarisation superposition state $|H\rangle_c + |V\rangle_c$. At the PBS, this state is converted into a path superposition. $|H\rangle_c$ takes the shorter path S, and after being coupled into a SMF-28 single-mode fibre, it travels directly to the optical switch, where it arrives at the lower entrance.
Conversely, $|V\rangle_c$ is reflected at the PBS and therefore takes the longer path L. It passes through a HWP with its fast axis oriented at 45°, which rotates the polarisation to H. It then enters a ~ 308 m long fibre spool, delaying its arrival time at the optical switch by $\Delta t \approx 151$ns. The switch must be triggered with an electric pulse at the correct moment, enabling it to switch into the parallel configuration and direct the delayed photon to its upper exit. When the switch is passively in the cross-configuration, the first photon arrives at this exit without additional switching. Any photon that leaves the switch through the lower exits will be discarded via the open end of a fibre circulator (not shown in this sketch; see figure 3.1). Once both photons have passed through the switch, the path superposition is converted into a time-bin superposition $|S\rangle_C + |L\rangle_C$.

3.4 Polarization compensation

While free-space propagation leaves the polarization of photons unaffected, every path through fiber induces a random polarization rotation. Although this experiment utilises single-mode fiber with low birefringence, stress factors such as bending can reduce the circular symmetry of the fiber core, resulting in this effect [32].
When working with polarization-encoded qubits, reversing these rotations becomes essential. Paddle-based polarization controllers are a commonly used tool for this purpose. They function by looping the fiber around spools, which then approximate half-wave or quarter-wave plates. The type of waveplate generated depends on the number of loops, as the induced birefringence is proportional to this number. Rotating the paddles results in a rotation of the fast axis, which lies in the plane of the spool [33].

3.4.1 Polarization compensation by rotating to identity

For this experiment, a compensation method was employed that allows for the decoupled compensation of two bases by adding a set of waveplates to the path and controlling the input and output polarization via polarization filters, as described in [32].
Since the photon source is shared among several users, it was necessary to modify this method slightly so that the waveplate set could be moved from the input of the fiber to a position behind the output coupler. This adjustment ensures that one user does not interfere with the individual compensation of the output paths of other users.
Given that the overall working principle remains the same for both variants, only the adjusted method will be described here.
Due to the narrow full width at half maximum (FWHM) of the photons' wavelength compared to the dispersion of an SMF-28 fiber, all random rotations can be considered unitary operations that preserve the purity of the polarization state. This implies that these rotations can be reversed by another unitary operation. By summing up all random rotations into a single unitary operation U, successful compensation depends on finding a unitary W such that:

$$WU\left|H\right\rangle = \left|H\right\rangle \tag{3.31}$$

$$WU\left|+\right\rangle = \left|+\right\rangle \tag{3.32}$$

meaning that W and U together form an identity operation $WU = I$. As long as they are not parallel on the Bloch sphere, one can choose freely any two states [23]. For this experiment $\left|H\right\rangle$ and $\left|+\right\rangle$ were used.
A polarizer is placed in front of the fibres input coupler and another behind the output coupler to ensure control over the input and output states. A segment of the fiber is looped through a three-paddle polarization controller, creating loops that first form a half-wave plate, then a half-wave plate, and finally a second quarter-wave plate. In the free space section behind the output coupler, a quarter-wave plate is set at an arbitrary angle, followed by a quarter-wave plate positioned between the half-wave plate and the

output polarizer.
The quarter-wave plate is fixed with its fast axis rotated by 45°, such that it rotates circularly polarised light but leaves diagonally polarised light unchanged. The half-wave plate can be set to an arbitrary angle.
For the first basis, the input polarizer is set to $|H\rangle$ and the output polarizer to $|V\rangle$. This configuration optimises polarization compensation when the single counts in the vertically polarised path are minimised. The paddles of the polarization controller are then rotated until the counts at the vertical output are minimised. Under optimal conditions, these counts reach the dark count level.
Once this is achieved, the input polarizer is rotated to $|+\rangle$ and the output polarizer to $|-\rangle$. The counts from vertical polarised photons are minimised again, but this time by rotating the half-wave plate. This adjustment sets the output state of the fiber to $|+\rangle$, allowing it to pass through the quarter-wave plate without polarization changes and be absorbed by the final polarising filter.
When the polarizers are rotated back to the computational basis, the compensation has likely been partially undone. By repeating the process, the compensations of both bases converge to a shared optimum.[32] Along the setup, the configuration of the compensation was realised either as shown in figure 3.8 or in the arrangement originally described in [32]. The only difference is the positioning of the waveplates, either in front of or behind the fibre section. The order of the waveplates and the procedure remain the same for both versions.

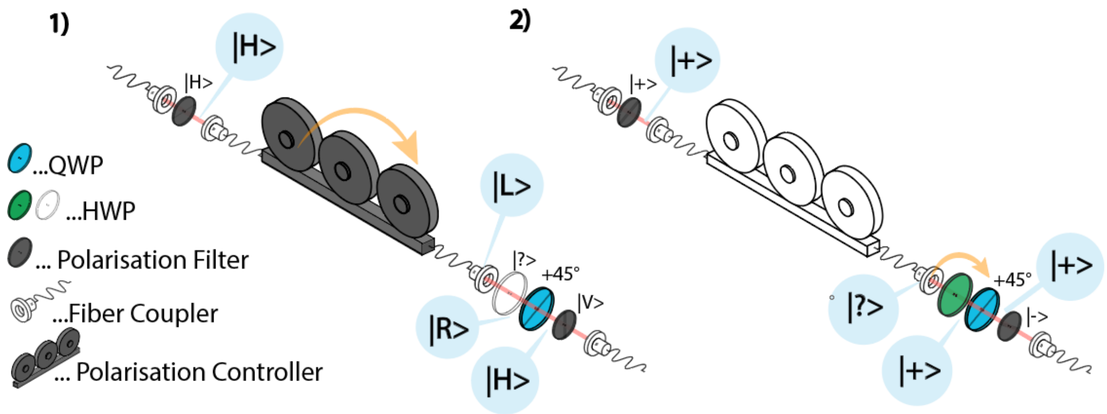

Figure 3.8: **The Compensation Setup:** it contains two polarizers, one HWP, one QWP, fixated at 45° and one polarization controller. 1) the input polarizer is turned to $|H\rangle$, the output polarizer to $|V\rangle$. Only the paddles of the polarization controller get turned, while the HWP remains untouched. 2) now the input polarizers are set to $|+\rangle$ and $|-\rangle$ and the paddles are kept in the final position of the first step while the HWP is turned.

3.4.2 Compensating for the ideal source output state

Most of the fibre sections in the setup are polarisation compensated using the method described above (3.4.1). However, for the single-mode fibres directly connected to the DWDM output channels, a different method has been applied, which will be outlined here.
The reason for this is that the maximally entangled two-photon state from the source is not necessarily the exact $|\Phi^+\rangle$ Bell state. It could, for instance, be phase-shifted. It is also possible, that single photons not correlated to the entangled pair could leak into one of the DWDM channels, as they may not perfectly overlap with one wavelength pair from the source. This method also aids in finding the correct setting for the HWP, which controls the pump polarisation, to approach the desired Bell state as closely as possible. However, for a coarse, preliminary setting, one round of compensation using the method from **??** is performed. A polarisation filter set to H is placed directly in front of the output fibre coupler at the source.
The movable mirrors are positioned into the paths of the interferometer in the time-bin creation section of the setup, directing the photons straight to the Tomography stage for Charlie-0. With a PBS in each Tomography setup of Charlie-0 and Bob, no additional polarisation filter is required at the fibre outputs. In Bob's setup, a HWP and a QWP are placed behind the input coupler, but no extra waveplates are needed in the time-bin section, as the idler photon sent to Bob and the signal photon travelling to the interferometer share a common phase. As a result, compensating the idler photon's phase will automatically correct the phase for both photons. It must be ensured that the motorised waveplate sets in the Tomography stages are rotated to the computational basis.
Now, the paddles of both sections are adjusted until the single counts in the reflected paths of both tomography stages are minimised. This roughly ensures that the polarisation of both photons undergoes an identity operation in the computational basis as they pass through the fibres. There is no need to perform the phase-compensation step at this stage, as the phase will be addressed later in the process.
Once this is complete, the polarisation filter can be removed from the source setup, and from this point onward, only coincidence counts will be considered.
The pump-HWP is then rotated until the number of $|VV\rangle_{C_0,B}$ or $|HH\rangle_{C_0,B}$ coincidences between Charlie-0 and Bob is minimised. It has been found that minimising the state with the highest potential coincidence rate is most effective. Therefore, it is useful to rotate the HWP further and compare the maximum rates for both states. In this setup, $|VV\rangle_{C_0,B}$ consistently reached the higher maximum, so this state was minimised. Afterwards, the polarisation control paddles for the signal and idler fibres are adjusted again until the coincidence rates between the cross terms $|VH\rangle_{C_0,B}$ and $|HV\rangle_{C_0,B}$ are as close to zero as possible. Under ideal conditions, only $|HH\rangle_{C_0,B}$ will show a coincidence rate above 0 Hz.

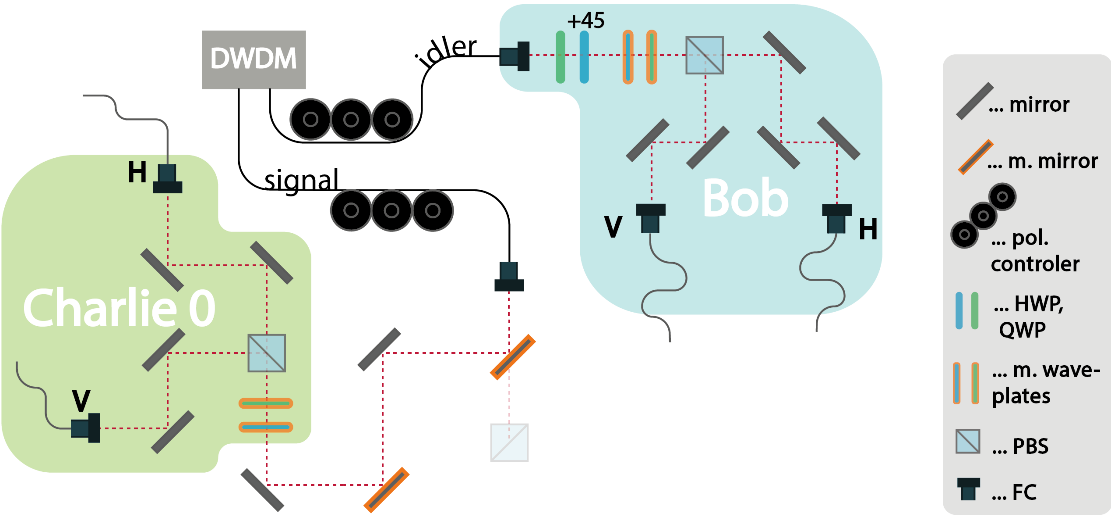

Figure 3.9: **Simplified sketch of the setup configuration for polarisation compensation on the SPDC source:** The signal photon is sent into the time-bin interferometer section, where the motorised mirrors have been positioned, allowing the light to take a shortcut to Charlie-0's tomography setup. The idler photon is sent to Bob as usual. Each tomography stage contains a set of motorised waveplates (one QWP and one HWP), a PBS, and a fibre coupler (FC) for each path from the PBS. Bob's section includes an additional set of manually adjusted waveplates, with the QWP fixed at 45°. These two waveplates are used to compensate the phase of the entangled state.

Now, the pump-HWP is rotated again until the coincidence rates of $|VV\rangle_{C_0,B}$ and $|HH\rangle_{C_0,B}$ are equal. Next, the motorised waveplates in both tomography stages must be rotated to the diagonal basis. If this basis is already partially polarisation-compensated, the coincidence rate should change according to the generated Bell state. For a $|\Phi^+\rangle$-state, coincidences are still expected between $|VV\rangle_{C_0,B}$ and $|HH\rangle_{C_0,B}$ when measured in the diagonal basis, whereas for a $|\Phi^-\rangle$-state, the pattern should invert, with the majority of coincidences between $|VH\rangle_{C_0,B}$ and $|HV\rangle_{C_0,B}$.
Since the pump is set to $|+\rangle_p$, we expect the source to produce $|\Phi^+\rangle_{C_0,B}$. Therefore, the HWP in Bob's tomography stage is rotated until the coincidences between $|VH\rangle_{C_0,B}$ and $|HV\rangle_{C_0,B}$ are minimised. Once this is achieved, the coincidences between $|VV\rangle_{C_0,B}$ and $|HH\rangle_{C_0,B}$ should reappear and remain stable, even when the motorised waveplates are rotated back to the computational basis. Typically, this is already sufficiently fulfilled after one round. If the desired result isn't achieved, it's best to repeat all the steps, including the preliminary round, since each step relies on the previous one and repeating or skipping steps individually will often worsen the outcome.

3.5 Two-qubit tomography

Quantum state tomography allows the reconstruction of a complete quantum wave function by a series of measurements on a large enough number of identically prepared quantum systems [34]. For two-qubit tomography, this method is applied to the joint state between two quantum systems.
This section describes the method of two-qubit tomography on the polarisation state of a photon pair and how this has been used to characterise the state from the SPDC source. The goal of quantum state tomography is to find the density matrix $\hat{\rho}$ of the system. A density matrix (or density operator) allows a description of the quantum system from which any expectation value of any operator can be derived. Additionally, it provides information about the purity and quantumness (such as entanglement) of the quantum state [35, pp. 46–51].
The density matrix of an arbitrary quantum state is given by the set of pure states $|\psi_i\rangle$ and their measurement probability p_i, with i as the number of states. The system given by the ensemble of pure states $\{p_i, |\psi_i\rangle\}$ can then be written as[36, p. 99]

$$\hat{\rho} \equiv \sum_i p_i \, |\psi_i\rangle\langle\psi_i| \, . \tag{3.33}$$

In order to be a valid density matrix of the system $\{p_i, |\psi_i\rangle\}$ $\hat{\rho}$ must satisfy the following two conditions:

1. **Trace condition:** the trace is equal to one.

$$Tr(\hat{\rho}) = \sum_i p_i tr(|\psi_i\rangle\langle\psi_i|) = \sum_i p_i = 1 \tag{3.34}$$

2. **Positivity condition:** For an arbitrary vector in state space $|\varphi\rangle$ the positivity condition is fulfilled if

$$\langle\varphi| \, \hat{\rho} \, |\varphi\rangle = \sum_i p_i \, \langle\varphi|\psi_i\rangle\langle\psi_i|\varphi\rangle = \sum_i p_i |\langle\varphi|\psi_i\rangle| \geqslant 0 \tag{3.35}$$

By this condition it is ensured, that any density operator provides a valid probability distribution and can be decomposed in the form

$$\hat{\rho} = \sum_j = \lambda_j \, |j\rangle\langle j| \tag{3.36}$$

with orthogonal vectors $|j\rangle$ and eigenvalues λ_j [36]. A density matrix also allows the distinction between mixed and pure states. For any pure state the trace of the density operator is equal to the trace of the squared operator and therefor holds

$$Tr(\hat{\rho}) = Tr(\hat{\rho}^2) = 1 \ . \tag{3.37}$$

While for a mixed state the trace of the squared operator will always be lower then one

$$Tr(\hat{\rho}^2) < Tr(\hat{\rho}) = 1 \ . \tag{3.38}$$

The more mixed a quantum state is, the lower its value $Tr(\hat{\rho}^2)$ will tune out and a state is maximally mixed if

$$\mathrm{Tr}\left(\hat{\rho}_{mix}^2\right) = \frac{1}{d} > 0 \ , \tag{3.39}$$

with d as the dimension of the system [37].
The concurrence C is a measure of the entanglement E of a state. It ranges from zero, for a completely separable state, to one ,for maximally entangled stated, in a monotone relation to E. In order to derive C from the density matrix, the "magic basis" must be introduced, which is composed from Bell-sates with additional phases [38]:

$$\begin{aligned}
|e_1\rangle &= \frac{1}{2}(|HH\rangle + |VV\rangle) \\
|e_2\rangle &= \frac{i}{2}(|HH\rangle - |VV\rangle) \\
|e_3\rangle &= \frac{i}{2}(|HV\rangle + |VH\rangle) \\
|e_4\rangle &= \frac{1}{2}(|HV\rangle - |VH\rangle).
\end{aligned} \tag{3.40}$$

The concurrence of a pure state in this basis $|\psi\rangle = \sum_i \alpha_i |e_i\rangle$ is then simply given by [38]

$$C(|\psi\rangle) = \left|\sum_i \alpha_i^2\right|. \tag{3.41}$$

For an arbitrary two-qubit state, it relates to the matrix R that is constructed from $\hat{\rho}$ expressed in the magical basis and its complex conjugate $\hat{\rho}^* = \sum_i j \, |e_i\rangle\langle e_j| \, \hat{\rho} \, |e_i\rangle\langle e_j|$ (which is the equivalent to a spin flip state as described in [39]) :

$$R(\hat{\rho}) = \sqrt{\sqrt{\hat{\rho}}\hat{\rho}^*\sqrt{\hat{\rho}}}. \tag{3.42}$$

R can be seen as a measure of the "degree of equality" between $\hat{\rho}$ and $\hat{\rho}^*$ via its trace, $0 \leqslant \mathrm{Tr}(R) \leqslant 1$, thereby providing a value for how well $\hat{\rho}$ represents a mixture of generalised Bell states. The concurrence is then given by

$$C = max(0, \lambda_{max} - Tr(R)) \ , \tag{3.43}$$

with λ_{max} as the biggest eigenvalue of R [38].

3.5.1 General reconstruction of a two-qubit density matrix

The general density matrix of a n-qubit state can be written as

$$\hat{\rho} = \frac{1}{2^n} \sum_{i_1,i_2,\ldots i_n=0}^{3} r_{i_1,i_2,\ldots i_n} \hat{\sigma}_{i_1} \otimes \hat{\sigma}_{i_2} \otimes \ldots \otimes \hat{\sigma}_{i_n} \tag{3.44}$$

With 4^n parameters $r_{i_1,i_2,...i_n}$. Due to normalisation, it must be ensured that $r_{0,0,...0} = 1$. Thus, $4^n - 1$ parameters are required for the estimation of ρ [40]. $\hat{\sigma} i_1 \ldots \hat{\sigma} i_n$ represent the Pauli operators acting on the nth qubit

$$
\begin{aligned}
\hat{\sigma}_0 = \hat{\mathcal{I}} &= \begin{pmatrix} 1 & 0 \\ 0 & 1 \end{pmatrix}, \; \hat{\sigma}_1 = \hat{\sigma}_x = \begin{pmatrix} 0 & 1 \\ 1 & 0 \end{pmatrix}, \\
\hat{\sigma}_2 = \hat{\sigma}_y &= \begin{pmatrix} 0 & -i \\ i & 0 \end{pmatrix}, \; \hat{\sigma}_3 = \hat{\sigma}_z = \begin{pmatrix} 1 & 0 \\ 0 & -1 \end{pmatrix}.
\end{aligned}
\tag{3.45}
$$

For this experiment, we are interested in the tomography of a two-qubit polarisation state. Therefore, 15 parameters r_{i_1,i_2} have to be determined for a density matrix of the form

$$
\hat{\rho} = \frac{1}{4} \sum_{i_1,i_2=0}^{3} r_{i_1,i_2} \hat{\sigma}_{i_1} \otimes \hat{\sigma}_{i_2} \; . \tag{3.46}
$$

For a single polarisation qubit the density matrix can be simply derived via

$$
\hat{\rho} = \frac{1}{2} \sum_{i=0}^{3} S_i \hat{\sigma}_i \;\; \text{with} \;\; S_i = Tr(\hat{\sigma}_i \hat{\rho}) \tag{3.47}
$$

and the Stokes parameters S_0, S_1, S_2, S_3 allow an intuitive visualisation of the state on the Bloch sphere.
Unfortunately, for the two-qubit case, such an intuitive picture is no longer possible, but the overall method is similar. While a single qubit can be fully described by four projective measurements $\hat{\mu}_0 = |H\rangle\langle H| + |V\rangle\langle V|$, $\hat{\mu}_1 = |H\rangle\langle H|$, $\hat{\mu}_2 = |D\rangle\langle D|$, and $\hat{\mu}_3 = |R\rangle\langle R|$, an equivalent set of 16 measurements $\hat{\mu}_i \otimes \hat{\mu}_j$ $(i,j = 0,1,2,3)$ is required for the reconstruction of a two-qubit state [40].
The outcomes n_{i_1}, n_{i_2} of these measurements are given by

$$
n_{i_1}, n_{i_2} = \mathcal{N} Tr[\hat{\rho}(\hat{\mu}_i \otimes \hat{\mu}_j)], \tag{3.48}
$$

with the data depending proportional factor $\mathcal{N}$. With a look at 3.47 this equation can be rewritten with as

$$
n_{i_1}, n_{i_2} = \frac{\mathcal{N}}{4} \sum_{j_1,j_2=0}^{3} = Tr(\hat{\mu}_{i_1} \hat{\sigma}_{j_1}) Tr(\hat{\mu}_{i_2} \hat{\sigma}_{j_2}) r_{i_1} r_{i_2}. \tag{3.49}
$$

Each measurement $\hat{\mu}_i$ is a linear combination of the Pauli operators (3.45) and via the elements Υ_{ij} of the matrix Υ they can be expressed as $\hat{\mu}_i = \sum_{j=0}^{3} \Upsilon_{ij} \hat{\sigma}_j$. The matrix Υ and it's left-inverse Υ^{-1} fulfil $\sum_{k=0}^{3} (\Upsilon^{-1})_{ik} \Upsilon_{kj} = \delta_{ij}$ (where δ_{ij} is the Kronecker delta) and are defined as [40]

$$
\Upsilon = \begin{pmatrix} 1 & 0 & 0 & 0 \\ 1/2 & 1/2 & 0 & 0 \\ 1/2 & 0 & 1/2 & 0 \\ 1/2 & 0 & 0 & 1/2 \end{pmatrix} \;\; \text{and} \;\; \Upsilon^{-1} = \begin{pmatrix} 1 & 0 & 0 & 0 \\ -1 & 2 & 0 & 0 \\ -1 & 0 & 2 & 0 \\ -1 & 0 & 0 & 2 \end{pmatrix}. \tag{3.50}
$$

Now, considering $Tr(\hat{\sigma}_i\hat{\sigma}_j) = 2\delta_{ij}$, equation 3.49 can be expressed as

$$n_{i_1}, n_{i_2} = \mathcal{N} \sum_{j_1,j_2=0}^{3} \Upsilon_{i_1j_1}\Upsilon_{i_2j_2} r_{i_1} r_{i_2}. \tag{3.51}$$

This now directly connects the previously arbitrary parameters $r_{i_1}r_{i_2}$ with the measurement quantities n_{i_1}, n_{i_2} which allows the derivation of the two-photon Stokes parameter S_{i_1,i_2} [40]:

$$\mathcal{N} r_{i_1} r_{i_2} = \sum_{j_1,j_2=0}^{3} (\Upsilon^{-1})_{i_1j_1}(\Upsilon^{-1})_{i_2j_2} n_{i_1}, n_{i_2} \equiv S_{i_1,i_2} \tag{3.52}$$

With the earlier mentioned relation $r_{0,0} = 1$, the first Stokes parameter is predefined as $S_{0,0} = \mathcal{N}$, and the density matrix of a two-qubit polarisation state is given in terms of the Stokes parameters as[40]

$$\hat{\rho} = \frac{1}{4} \sum_{i_1,i_2=0}^{3} \frac{S_{i_1,i_2}}{S_{0,0}} \hat{\sigma}_{i_1} \otimes \hat{\sigma}_{i_2} \tag{3.53}$$

While this definition gives a useful insight into the theoretical background of two-qubit tomography, from an experimental point of view, it's not the most practical approach. Instead, it's much more convenient to consider the measurement probabilities for the respective polarisation states of the single-photon Stokes parameters in the H/V-basis. [14]

$$\begin{aligned} S_0 &= P_{|H\rangle} + P_{|V\rangle}, \\ S_1 &= P_{|D\rangle} - P_{|A\rangle}, \\ S_2 &= P_{|R\rangle} - P_{|L\rangle}, \\ S_3 &= P_{|H\rangle} - P_{|V\rangle}, \end{aligned} \tag{3.54}$$

where $P_{|\varphi\rangle}$ is the measurement probability of the state $|\varphi\rangle$. For example the Stokes parameter $S_{3,3}$ of the Bell state Φ^+ is then simply given by

$$\begin{aligned} S_{3,3} &= S_3 \otimes S_3 = (P_{|H\rangle} - P_{|V\rangle}) \otimes (P_{|H\rangle} - P_{|V\rangle}) \\ &= P_{HH} - P_{HV} - P_{VH} + P_{VV} \\ &= \frac{1}{2} - 0 - 0 + \frac{1}{2} \\ &= 1 \end{aligned} \tag{3.55}$$

This procedure can be done with any orthogonal basis $|\varphi\rangle, |\varphi^{\perp}\rangle$. For example, if the first qubit had been measured in this arbitrary basis, the Stokes parameter above could be obtained by calculating $S_{3,3} = (P_{|\varphi\rangle} - P_{|\varphi^{\perp}\rangle}) \otimes (P_{|H\rangle} - P_{|V\rangle})$.

Even though the reconstruction of a two-qubit state requires the measurement of 16 Stokes parameters, it's enough to measure only nine of them directly, as the parameters $S_{j,0}, S_{0,j}$ can be derived from the measurements of $S_{i,j}$ $(ij = 1, 2, 3)$ and the first parameter is constant as $S_{0,0} = 1$ [14].

3.5.2 State Projection

For the measurement of a two-qubit tomography, the signal and idler photons are measured separately in a setup consisting of one HWP, one QWP, and one PBS, known as a tomography stage. As the PBS splits the polarisation state into $|H\rangle$ and $|V\rangle$ polarisation states, it is necessary to adjust the waveplates to project onto the required basis, ensuring that the correct outcome is measured. In our setup, both PBS outputs are connected to detectors, which has the advantage of providing the total number of counts for every basis, thus increasing the accuracy of the tomography results. The required waveplate rotation of an angle ϕ can be expressed as a unitary transformation. For the H/V-basis, these are given by [14]

$$\begin{aligned} U_{HWP}(\theta) &= \begin{pmatrix} \cos^2(\theta) - \sin^2(\theta) & 2\cos(\theta)\sin(\theta) \\ 2\cos(\theta)\sin(\theta) & \sin^2(\theta) - \cos^2(\theta) \end{pmatrix} \\ U_{QWP}(\theta) &= \begin{pmatrix} \cos^2(\theta) + i\sin^2(\theta) & (1-i)\cos(\theta)\sin(\theta) \\ (1-i)\cos(\theta)\sin(\theta) & \sin^2(\theta) + i\cos^2(\theta) \end{pmatrix} \end{aligned} \tag{3.56}$$

For tomography stages in the configuration as they are used in this experiment, and for a given observable A with eigenstates $|a_\pm\rangle$ and eigenvalues ± 1, the goal is to find an operation U that performs a projection in the form of [23, p. 63]

$$U|a_+\rangle = |H\rangle \quad \text{and} \quad U|a_-\rangle = |V\rangle \tag{3.57}$$

This represents a von Neumann measurement in which the positive eigenstate $|a_+\rangle$ is always transmitted through the PBS, while the negative eigenstate $|a_-\rangle$ is reflected. Unlike for arbitrary rotations, in this projection the relative phase can be neglected, simplifying the procedure and allowing operation with only two waveplates [23].
The projection state $|a_\pm\rangle$ must not be confused with the arbitrary incoming state; rather, it is the basis in which the incoming state will be measured.
First, the QWP must act to rotate the state $|a_\pm\rangle$ into the equatorial plane:

$$U_{QWP}(\theta)|a_+\rangle = \alpha|H\rangle + \beta|V\rangle, \tag{3.58}$$

with $\alpha, \beta \in \mathbb{R}$. Afterwards, the HWP rotates the state along the equator to $|H\rangle$:

$$U_{HWP}(\phi)(\alpha|H\rangle + \beta|V\rangle) = |H\rangle. \tag{3.59}$$

Once the respective angles θ and ϕ are determined, they will simultaneously transform $|a_-\rangle$ to $|V\rangle$, as the waveplates then apply the intended operation.

$$U|a_\pm\rangle = U_{HWP}(\phi)U_{QWP}(\theta)|a_\pm\rangle. \tag{3.60}$$

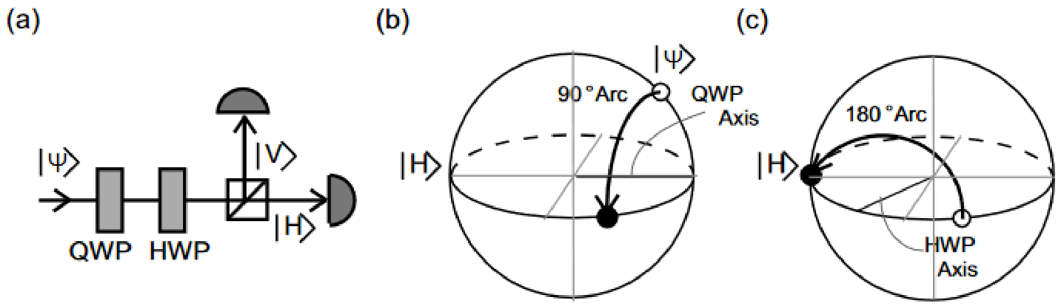

Figure 3.10: **Illustration of how an arbitrary state $|\Psi\rangle$ can be projected onto $|H\rangle$ using a HWP and a QWP:** (a) A schematic sketch of a tomography stage. (b) The projection state $|\Psi\rangle$ (not the incoming state) is rotated by the QWP into the linear polarisation plane. (c) The HWP then acts on the linear state, transforming it into $|H\rangle$. Adapted from: J.B.Altepeter, E.R. Jeffrey, and P.G. Kwiat *"Photonic State Tomography"*, Advances In Atomic, Molecular, and Optical Physics, 52, 2005[14, p. 26]

3.5.3 Testing Photon Sources and Setup via Quantum State Tomography

For this experiment, two-qubit tomography was used to evaluate the performance of the setup and to characterise the two-photon state generated by the SPDC source. Only when the tomography produced the desired $|\Phi^+\rangle$ state was it confirmed that the HWP in the source setup was rotated to the correct position, and that all waveplates in the tomography stages of Bob, Charlie-0, and Charlie-1 were functioning as expected. As the direct path to Charlie-1 is the least complex, the first tomography measurements were conducted between Charlie-1 and Bob. For this, the circulator was bypassed, and the signal output fibre was directly connected to the input fibre leading to Charlie-1's tomography stage. Subsequently, polarisation rotations in the fibres to both tomography stages were compensated simultaneously via the method described in section 3.4.2. Afterwards, the tomography measurements could begin. The waveplate angles, relative to their fast axis, for projecting the H/V, A/D, and R/L bases onto the PBS output states $|H\rangle$ and $|V\rangle$, as described in section 3.5.2, are as follows:

Basis	H/V	A/D	R/L
QWP	0°	45°	45°
HWP	0°	−22.5°	0°

Table 3.1: Wave plate angles with respect to the fast axis to project the respective basis onto $|H\rangle$ and $|V\rangle$

Here, A/D refers to diagonal (D) and antidiagonal (A) polarisation, while R/L denotes right (R) and left (L) circular polarisation. The associated basis vectors, expressed in terms of $|H\rangle$ and $|V\rangle$, are given by

$$\begin{aligned}
|D\rangle &= |+\rangle = \frac{1}{\sqrt{2}}(|H\rangle + |V\rangle) \\
|A\rangle &= |-\rangle = \frac{1}{\sqrt{2}}(|H\rangle - |V\rangle) \\
|R\rangle &= |+i\rangle = \frac{1}{\sqrt{2}}(|H\rangle + i\,|V\rangle) \\
|L\rangle &= |-i\rangle = \frac{1}{\sqrt{2}}(|H\rangle - i\,|V\rangle).
\end{aligned} \tag{3.61}$$

The first and second expression as ket-vectors are equally common. While the first refers to the polarisation state, the second is connected the Bloch sphere representation.
The set of nine measurements required for a two-qubit tomography (see 3.5.1) are

n	1	2	3	4	5	6	7	8	9
signal	H/V	H/V	H/V	A/D	A/D	A/D	R/L	R/L	R/L
idler	H/V	A/D	R/L	H/V	A/D	R/L	H/V	A/D	R/L

Table 3.2: Measurement basis of the signal and idler photon for each of the nine tomography measurements $n = 1 \ldots 9$.

The analysis was performed using the Python Tomography Library developed by the Kwiat Quantum Information Group [41]. This tool takes into account the coincidences between signal and idler photons as well as the single count rates, estimating the density matrix that is most likely to produce the observed data. It also ensures that the estimated density matrix represents a valid physical state. Without this correction, the calculated matrix might not satisfy the required conditions for trace and positivity (3.34, 3.35). Additionally, this library provides predefined functions to calculate the trace, purity, and concurrence.
Once the tomography between Charlie-1 and Bob yielded satisfactory results, the same procedure had to be repeated for the tomography between Charlie-0 and Bob. In order to measure directly with the tomography stage and avoid the rest of the setup, one mirror mounted on motorised translation stages is moved into the path of the time-bin interferometer. A second mirror is moved into the path to the tomography stage to align the beam correctly through the motorised waveplate set and the PBS (exactly the way as it is illustrated for the polarisation compensation in figure 3.9). Only when the tomography results are sufficiently similar we can confidently rely on all stages to operate consistently, ensuring their proper functioning together during the measurement of the SWITCH output.

3.6 The Commutation Game

This chapter addresses the experimental realisation of the commutation game, which has been theoretically described in section 2.2.1.
In the commutation game, the signal photon must enter the setup in $|+\rangle$-polarisation. The commutation game's success relies only on the quantum SWITCH's causal superposition and the measurement of a single photon passing through it. Therefore, it would be sufficient to prepare the signal photon in the state $|+\rangle$ (for example, by using a polarization filter) and to use the idler photon only as a herald. It's detection event can then serve as a time reference to trigger the optical switches.
However, since the entanglement between the signal and idler photons plays an important role in the subsequent measurement of the local causal inequality, we measure the herald photon in $|+\rangle$. With a resource state in $|\Phi^+\rangle$, this projects the signal photon into a $|+\rangle$-polarisation state. Since we are using here a new method to measure the control qubit, the commutation game measurement tests its functionality. Additionally we expect that if the setup can successfully perform the commutation game with the input state projected onto the signal through the measurement of the idler photon, it will also be able to violate the LCI.
Therefore, Bob's motorised waveplates are rotated such that they project the $|+/-\rangle$-basis onto $|H/V\rangle$. In the following we only consider coincidence events between Bob and Charlie when Bob measures a $|+\rangle$ state. Events when Bob measures $|-\rangle$ are discarded. Now all relevant signal photons enter the time-bin interferometer in $|+\rangle$ that is then converted into the time bin control qubit with a polarisation target qubit in $|H\rangle_T$. The state that enters the quantum SWITCH is therefore:

$$|\Psi\rangle_{in} = \frac{1}{\sqrt{2}}(|S\rangle + |L\rangle)_C \, |H\rangle_T \, . \tag{3.62}$$

For the commutation game, the setups of Alice-1 and Alice-2 are equipped with arbitrary unitary quantum channels, which are realized by sandwiching a HWP with two QWPs. Therefore, they can implement any arbitrary unitary operator, including the four Pauli operators $\hat{\mathcal{I}}$, $\hat{\sigma}_x$, $\hat{\sigma}_y$, and $\hat{\sigma}_z$.

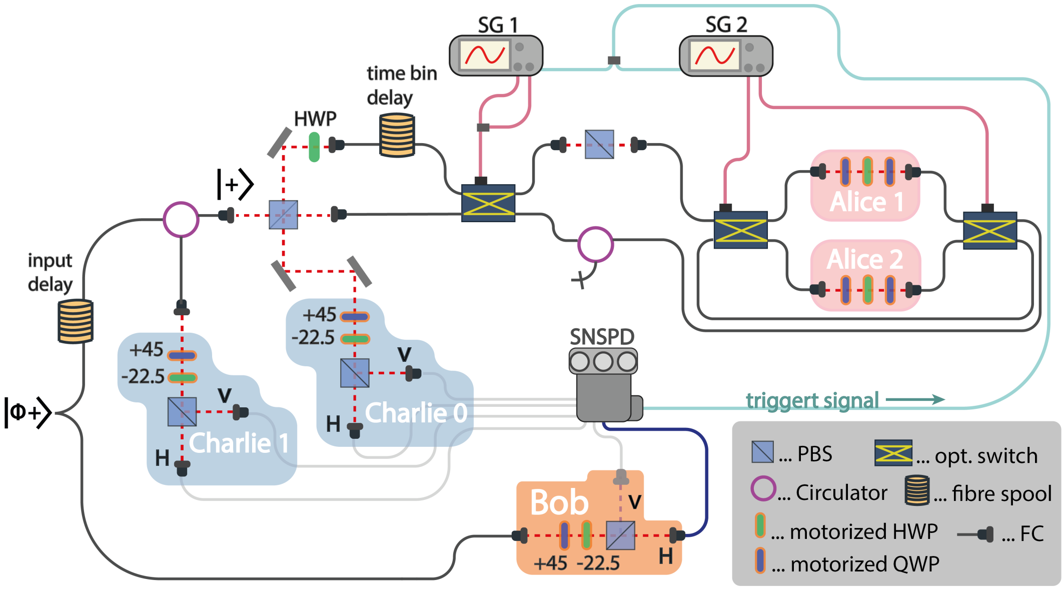

Figure 3.11: **Simplified illustration of the setup configuration for the commutation game:** The optical switches are triggered by the idler photon in Bob's H-path. His tomography waveplates project onto $|+/-\rangle$. Thereby, the signal photon enters the time-bin interferometer in $|+\rangle$. Equipped with two QWPs and a HWP, both Alices can set any Pauli operator. On the way back, the time bins unify at the PBS in the interferometer. With the HWPs at $-22.5°$ and the QWPs at $45°$ the tomography waveplates project $|+/-\rangle$ onto $|H/V\rangle$. With these waveplate-settings the PBS acts as a Hadamard gate on the incoming polarisation states.

The matrix representations of these unitary operators have already been introduced in equation 3.45. Every Pauli operator commutes with itself and $\hat{\mathcal{I}}$, while it anticommutes with any other Pauli operator.
After the SWITCH, when Alice-1 and Alice-2 have both applied one of the Pauli operators to the target state the total state, that exits the quantum SWITCH is given by

$$|\Psi\rangle_{out} = \frac{1}{\sqrt{2}}\big(|S\rangle_C\,|\psi_S\rangle_T + |L\rangle_C\,|\psi_L\rangle_T\big), \tag{3.63}$$

with

$$\begin{aligned}|\psi_S\rangle_T &= \alpha_S\,|H\rangle_T + \beta_S\,|V\rangle_T\,,\\ |\psi_L\rangle_T &= \alpha_L\,|H\rangle_T - \beta_L\,|V\rangle_T\,.\end{aligned} \tag{3.64}$$

Following the measurement principle described in 2.2.1, now a Hadamard gate $H = \frac{1}{\sqrt{2}}\left(\begin{smallmatrix}1 & 1\\ 1 & -1\end{smallmatrix}\right)$ is applied to the control qubit that transforms the output state to

$$|\Psi\rangle_{out} \xrightarrow{\text{H}} |\Psi'\rangle_{out} = \frac{1}{2}\Big[(|S\rangle + |L\rangle)_C\,|\psi_S\rangle_T + (|S\rangle - |L\rangle)_C\,|\psi_L\rangle_T\Big]. \tag{3.65}$$

Keeping in mind that $|S/L\rangle$ represent $|0/1\rangle$ for the control qubit, this state can be rearranged:

$$
\begin{aligned}
|\Psi'\rangle_{out}^{S/L} &= \frac{1}{2}(|\psi_S\rangle + |\psi_L\rangle)_T |S\rangle_C + \frac{1}{2}(|\psi_S\rangle - |\psi_L\rangle)_T |L\rangle_C \\
&= \frac{1}{2}\Big[\alpha_S |H\rangle + \beta_S |V\rangle + \alpha_L |H\rangle + \beta_L |V\rangle\Big]_T |S\rangle_C \\
&+ \frac{1}{2}\Big[\alpha_S |H\rangle + \beta_S |V\rangle - \alpha_L |H\rangle - \beta_L |V\rangle\Big]_T |L\rangle_C \\
&= \frac{1}{2} \underbrace{|S\rangle_C \Big[(\alpha_S + \alpha_L) |H\rangle + (\beta_S + \beta_L) |V\rangle\Big]_T}_{|0\rangle_C \{U_1,U_2\}|\psi\rangle_T} \\
&+ \frac{1}{2} \underbrace{|L\rangle_C \Big[(\alpha_S - \alpha_L) |H\rangle + (\beta_S - \beta_L) |V\rangle\Big]_T}_{|1\rangle_C [U_1,U_2]|\psi\rangle_T} .
\end{aligned}
\tag{3.66}
$$

with the respective terms of the output state from the commutation game $\frac{1}{2}|0\rangle_C \{U_1, U_2\} |\psi\rangle_T + \frac{1}{2}|1\rangle_C [U_1, U_2] |\psi\rangle_T$ (2.15). This way it shows that here the first therm contains the anti-commuting relation, and the second therm the commuting relation:

$$(\alpha_S + \alpha_L) |H\rangle_T + (\beta_S + \beta_L) |V\rangle_T = \{U_1, U_2\} |\psi\rangle_T \,, \tag{3.67}$$

$$(\alpha_S - \alpha_L) |H\rangle_T + (\beta_S - \beta_L) |V\rangle_T = [U_1, U_2] |\psi\rangle_T \,. \tag{3.68}$$

Thus by the measurement probabilities of $|S\rangle_C$ and $|L\rangle_C$ one can tell if the unitary operators set by Alice-1 and Alice-2 commute or anticommute:

$$P_{|S\rangle} = \frac{|\alpha_S + \alpha_L|^2}{4} + \frac{|\beta_S + \beta_L|^2}{4} \;\rightarrow\; U_1, U_2 \text{ commute,} \tag{3.69}$$

$$P_{|L\rangle} = \frac{|\alpha_S - \alpha_L|^2}{4} + \frac{|\beta_S - \beta_L|^2}{4} \;\rightarrow\; U_1, U_2 \text{ anticommute.} \tag{3.70}$$

Now this ideal outcome has to be adapted to the experimental setup: As mentioned in 3.1.1 the time-bin SWITCH is synchronised such that the time bins travel back in that path, that they did not take on their way in. Meaning that the short time bin now travels the long way and vice versa. Thereby the polarisation of $|S\rangle_C$ is flipped when it passes the HWP at 45° in the long arm. Considering this the state right before the photon arrives at the interferometer-PBS is

$$|\Psi\rangle_{out} = \frac{1}{\sqrt{2}}\Big[(\alpha_S |V\rangle + \beta_S |H\rangle)_T |S\rangle_C + (\alpha_L |H\rangle + \beta_L |V\rangle)_T |L\rangle_C\Big]. \tag{3.71}$$

The PBS not only unifies the time bins but also acts as a Hadamard gate when the output is later measured in the $|+/-\rangle$ basis. Since the time bins arrive from different directions

at the PBS, it separates them differently depending on their polarisation state. For the former $|S\rangle_C$ time bin, the transmitted path leads to Charlie-0, where its H-polarised photons arrive, while the vertical polarisation is reflected and ends up at Charlie-1's tomography setup.
The former $|L\rangle_C$ meets the PBS from the side orthogonal to the entrance of $|S\rangle_C$; thus, its polarisation state is sorted in the opposite manner, with $|H\rangle_T$ reaching Charlie-1 and $|V\rangle_T$ ending in Charlie-0's tomography stage:

$$\text{Charlie-0: } \frac{1}{\sqrt{2}}(\beta_S |H\rangle + \beta_L |V\rangle) \tag{3.72}$$

$$\text{Charlie-1: } \frac{1}{\sqrt{2}}(\alpha_S |V\rangle + \alpha_L |H\rangle) \tag{3.73}$$

When both measure in the $|+/-\rangle$ basis they obtain the states

$$\text{Charlie-0: } \overbrace{\frac{1}{2}(\beta_S + \beta_L)}^{C_0} |H\rangle + \overbrace{\frac{1}{2}(\beta_S - \beta_L)}^{A_0} |V\rangle, \tag{3.74}$$

$$\text{Charlie-1: } \underbrace{\frac{1}{2}(\alpha_S + \alpha_L)}_{C_1} |V\rangle + \underbrace{\frac{1}{2}(\alpha_S - \alpha_L)}_{A_1} |H\rangle. \tag{3.75}$$

By comparing the coefficients in the equations 3.69 and 3.70 one can see, that here the commuting and anti-commuting term for U_1, U_2 can be found in the form:

$$|C_0|^2 + |C_1|^2 \ \rightarrow U_1, U_2 \text{ commute,} \tag{3.76}$$

$$|A_0|^2 + |A_1|^2 \ \rightarrow U_1, U_2 \text{ anticommute.} \tag{3.77}$$

To avoid confusion it might be useful to point out, that these terms do not represent the probability for commutation or anticommutation, yet are the experimental equivalents to $[U_1, U_2]$ and $\{U_1, U_2\}$. Meaning that when Alice-1's and Alice's operators e.g. commute, they fulfil $[U_1, U_2] = 0$ and therefore $|C_0|^2 + |C_1|^2 = 0$, which means that there can only occur clicks in Charlie-0's $|V\rangle$ and in Charlie-1's $|H\rangle$ detector. In the original commutation game, the photon leaves port-0 when the operators commute and port-1 when they anticommute. As an analogy it can be seen here as if Charlie-1's H-path and Charlie-0's V-path form here together port-0 and port-1 is represented by the sum of Charlie-0's H-path and Charlie-1's V-path (illustrated in figure 3.12).
For the measurement of the commutation game, all possible combinations of the Pauli operators should be tested. For each of these operator pairs the coincidences between Charlie-0 and Bob, as well as for Charlie-1 and Bob are detected.

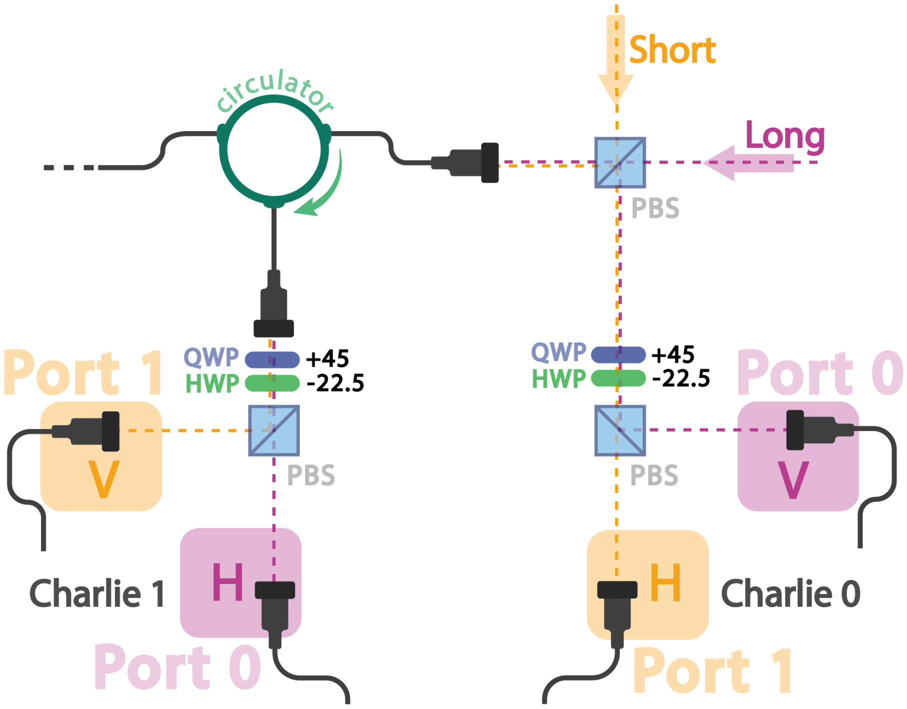

Figure 3.12: **Illustration of how the qubits are sorted after their return from the quantum SWITCH:** The former time-bin control qubits are unified at the PBS in the interferometer. The vertical component of the polarisation qubit, which was carried by the long path ($|L\rangle_c$), is reflected into Charlie-0's tomography stage, while the vertical component is transmitted and arrives at Charlie-1. This splitting occurs in the opposite manner for the former short time bin ($|S\rangle_c$). Thus, both of Charlie's tomography stages measure a portion of each control qubit while simultaneously measuring the polarisation of the target qubit. With the waveplates set to the diagonal basis, the PBS in the interferometer acts as a Hadamard gate. Referencing the original commutation game (2.2.1), the purple-highlighted detectors form port-0, and the orange-highlighted detectors represent port-1.

4 Results

This chapter will present the measurement results for the preliminary measurements that had to be done to characterise the setup and the source as well as the results of the commutation game.

4.1 Setup Characterisation

We only use the two most efficient wavelength pairs from the source for our experiments which end up in the DWDM channels $C32, C36$ and $C33, C35$. Since we rely on these channels to work as intended it had to be controlled, that they return the right wavelengths with minimal overlap to the neighbouring channels and conserve the purity of the polarisation states:

DWDM-Channel	λ $[nm]$ ± 0.020 nm	Degree of Polarisation $\pm$ 1.0 %
C32	1551.720	100.0 %
C33	1550.920	99.9 %
C35	1549.320	100.0 %
C36	1548.510	98.9 %

Table 4.1: The four DWDM channels, with their respective wavelengths, were measured for their degree of polarisation. The tunable CW laser was connected to the DWDM and set to the centre wavelength of each output channel, the degree of polarisation was measured with a Thorlabs polarimeter PAX1000IR2. The results show that the DWDM does not compromise the purity of the polarisation states.

λ [nm] ($\pm$ 0.02 nm)	1552.52 (C31)	1551.72 (C32)	1550.92 (C33)	1550.12 (C34)
C32	52.5 nW $\pm$ 1.6 nW	3.72 mW $\pm$ 0.12 mW	0.0900 nW $\pm$ 0.0027 nW	
C33		55.50 nW $\pm$ 0.17 nW	4.00 mW $\pm$ 0.12 mW	9.67 nW $\pm$ 0.30 nW

λ [nm] ($\pm$ 0.02 nm)	1550.12 (C34)	1549.32 (C35)	1548.51 (C36)	1547.72 (C37)
C35	33.1 nW $\pm$ 1.0 nW	4.12 mW $\pm$ 0.13 mW	0.1100 nW $\pm$ 0.033 nW	
C36		4.10 nW $\pm$ 0.13 nW	1.000 mW $\pm$ 0.030 mW	4.80 nW $\pm$ 0.15 nW

Table 4.2: Measurement of the power leakage into the DWDM channels from the wavelengths of neighbouring channels. For this, the tunable alignment laser was connected to the DWDM input fibre, set to the transmission wavelength of the respective channel. The power of this channel and the two neighbouring channels was then measured. As shown here, the leakage into the neighbouring channels is negligibly small.

For this setup $C35$ has been used as the idler and $C33$ as the signal photon. For the measurements of the two-qubit tomography the single count rate in each detector as well as the coincidence counts between all signal and idler detectors. The coincidence window, is the time frame in which the arriving photons are relevant for the measurement. A signal and an idler photon that arrive within this window are considered as one coincidence count. While a too large window enhances noise a too small window will cause losses. Here the coincidence window was estimated from the gaußian curve that is formed in a histogram when the coincidence counts are measured and roughly corresponds to six times the deviation from the mean $window_{cc} = 6 * \sigma = 647\ ps$.
Since all photons arrive at their detectors at different times this has to be corrected for at the time tagger by setting the right channel delays.

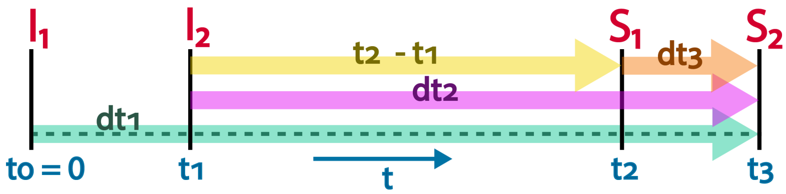

Figure 4.1: **Illustration of the channel delays:** t_0, t_1, t_2 and t_3 refer to the arrival times at the detectors of the photons I_1, I_2, S_1 and S_2, with I_1 arriving first and S_2 last. The delays dt_1 and dt_2 can be measured directly with a coincidence histogram of the respective channels.Here I_2 was chosen as the idler channel from which dt_3 is calculated. So dt_3 is given by the difference of dt_2 and the arrival time difference $t_2 - t_1$ that can simply be measured via a coincidence histogram with I_2 as the start- and S_1 as the stop-channel.

Otherwise no coincidences would appear in the measurement results. This has to be done for all measurement configurations individually by taking the histograms between all idler with all signal channels. The time at which the peak appears in such a histogram represents the difference of the arrival times between the two photons. In this setup the idler photons will always arrive earlier than the signal photons. Let's call the first and second detectors for the idler photon I_1 and I_2, with the photon arriving at times t_0 and t_1 at each detector, respectively. Similarly, for the signal photon, the first detector S_1 measures at t_2, and the second detector S_2 at t_3 The channel delay for the last arriving photon is always zero: $dt_{S2} = 0$. The delays dt_{I1} and dt_{I2} can be taken directly from center of the peak in the histogram between S_2 and the respective idler channel. Since there can't be any coincidences between S_1 and S_2, the delay dt_{S1} relies on a additional histogram between S_1 and one of the idler photons. It can then be calculated by the relative arrival time of that histogram and the delay time of the selected idler

$$dt_{S1} = dt_i - (t_2 - t_i). \tag{4.1}$$

Here t_i and dt_i revere to the chosen idler photon.

As described in section 3.5.1 it is important to ensure that all tomography stage operate as intended before any further measurements could be done. This was done by measuring the output source directly in each of Charlies Tomography stages combined with Bob. First this was done with the tomography stage of Charlie-1 and Bob. The channel delays for this tomography were:

Time Tagger Channel	Delay [ns]
4 (Charlie-1 V)	0
8 (Charlie-1 V)	0.141
1 (Bob V)	6.609
17 (Bob H)	7.884

Table 4.3: Settings for the internal channel delay in the time tagger for measuring the coincidences for the tomography on the source between Charlie-1'S and Bobs setups.

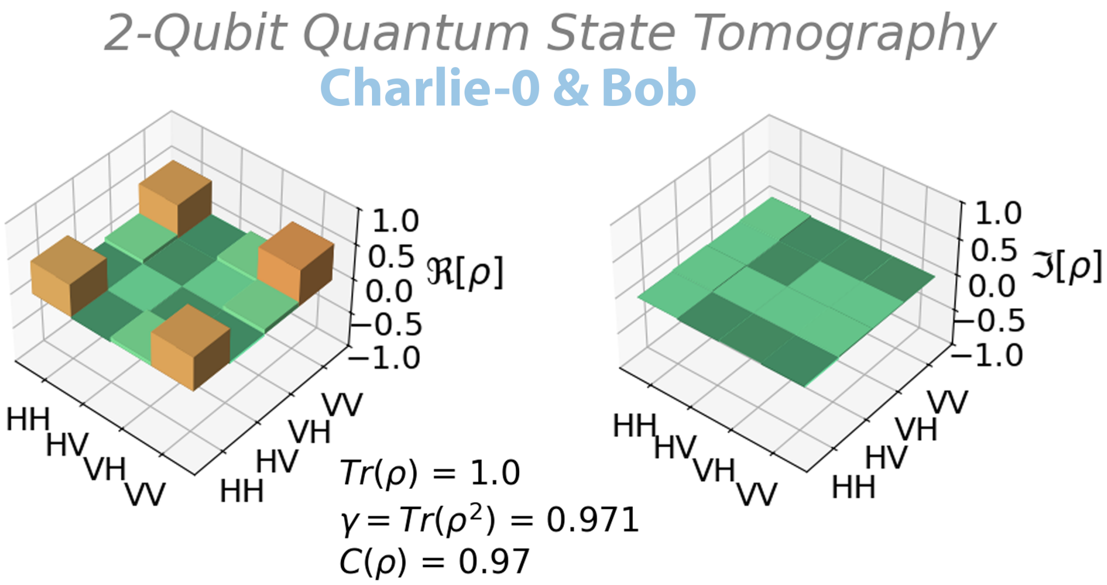

Figure 4.2: **Two qubit quantum state tomography on the source state measured between Charlie-0 and Bob:** Measured with an integration time of $t_{mes} = 10\ s$ and a coincidence window of $cc_{window} = 647\ ps$. For this measurement the movable mirrors were set into the input path of the time bin interferometer to guide the photons directly to Charlie-0's tomography stage.

Next this measurements have been repeated between Charlie-0 and Bobs setup. To exclude the rest of the signal setup, the motorised mirrors were moved into the paths as illustrated in figure 3.9. The channel delays for this configuration are:

Time Tagger Channel	Delay [ns]
4 (Charlie-1 V)	1.282
8 (Charlie-1 V)	0
1 (Bob V)	403.261
17 (Bob H)	403.394

Table 4.4: Settings for the internal channel delay in the time tagger for measuring the coincidences for the tomography on the source between Charlie-0'S and Bobs setups.

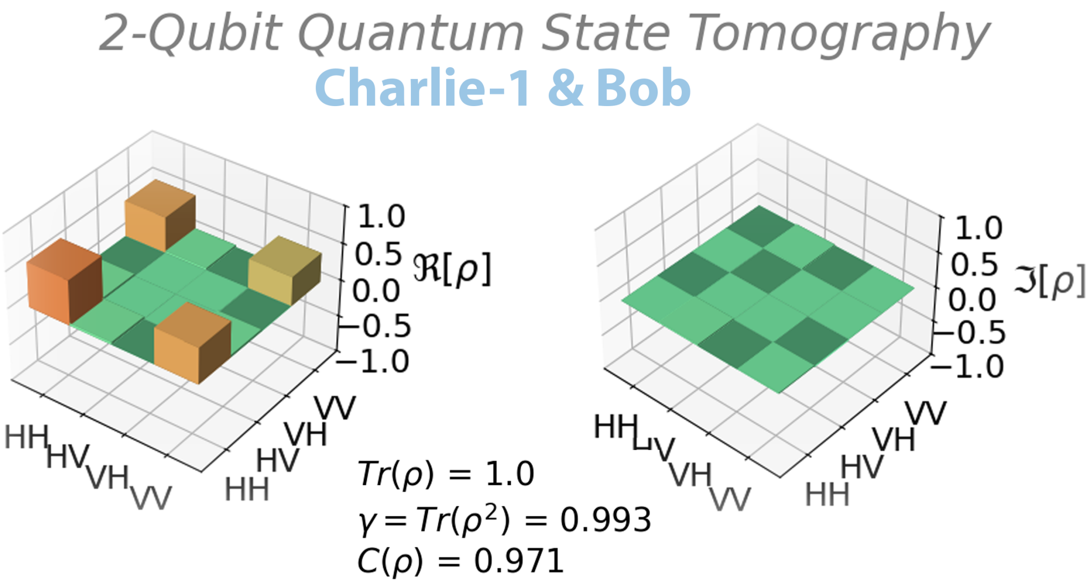

Figure 4.3: **Two qubit quantum state tomography on the source state measured between Charlie-1 and Bob:** The integration time was set to $t_{mes} = 10\ s$ and a coincidence window was again set to $cc_{window} = 647\ ps$. For this measurement the input circulator was bypassed and the source directly connected to to input fiber to Charlie-1's tomography stage.

The following measurement was done during the optimisation process of Charlie-0's setup to get a better understanding of the SPDC source setup:

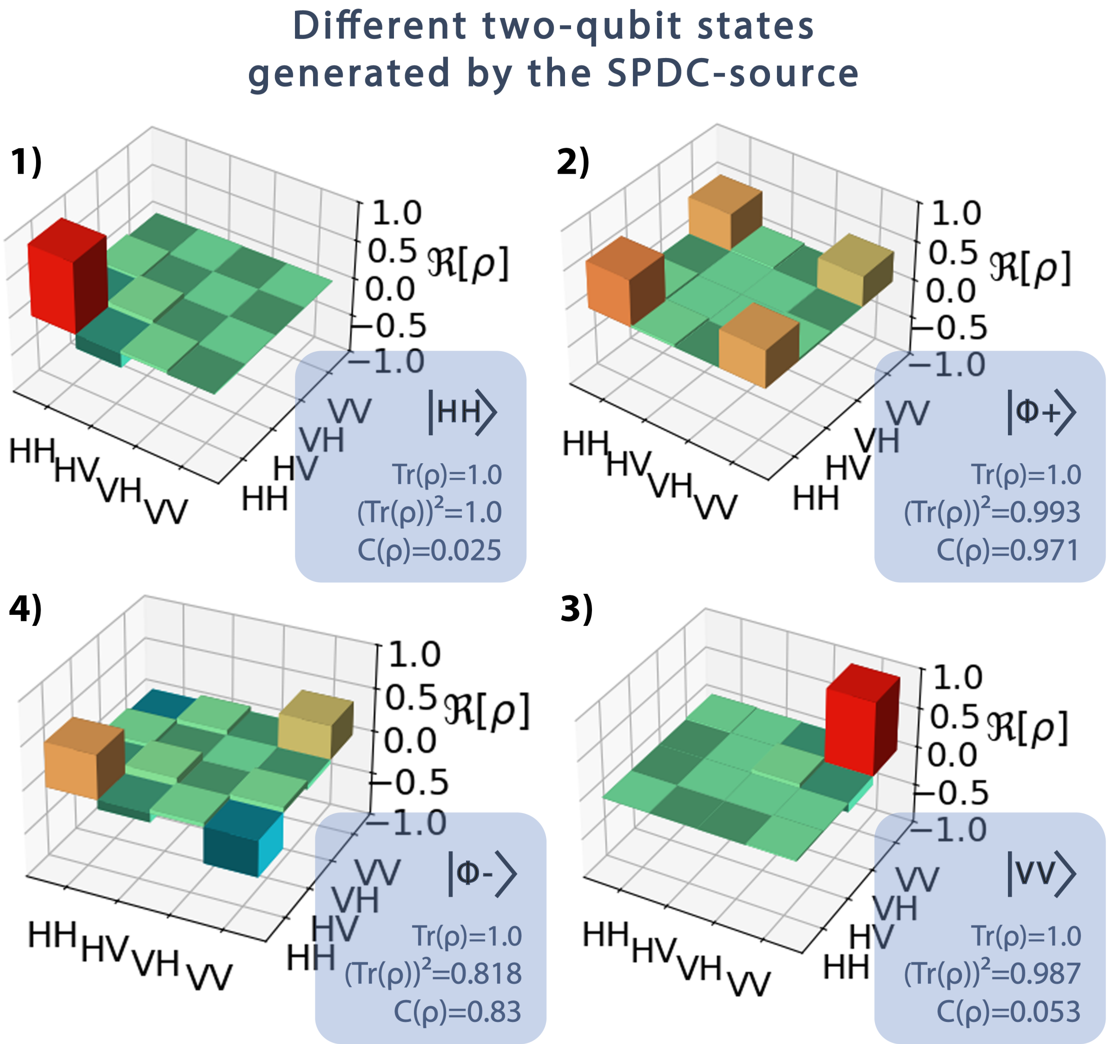

Figure 4.4: **Tomography of the source state with different settings of the pump HWP:** Beside 2) all results were reconstructed from coincidences between Charlie-0 and Bob measured with an integration time of $t_{mes} = 3\ s$. During the measurement of 2) the integration time was set to $t_{mes} = 10\ s$. The coincidence window for all measurements was $cc_{window} = 647\ ps$. 1) The Sagnac loop is pumped with $|V\rangle_{pump}$ and creates a pure, unentangled $|HH\rangle_{s,i}$ state. 2) Here the source was pumped with $|+\rangle_{pump}$ which lead to the creation of the Bellstate $|\Phi^+\rangle_{s,i}$). 3) With the HWP_{pump} rotated to $0°$, the pump polarisation is $|H\rangle_{pump}$ and the source creates a $|VV\rangle_{s,i}$ state. 4) When pumped with $|-\rangle_{pump}$ the source creates a $\Phi^-_{s,i}$ state. The measurements 1), 3) 4) were done before the tomography setup of Charlie-0 was in it's optimal configuration. While this doesn't show a strong effect on the separable states 1) and 3) it decreased the purity and concurrence of the reconstructed Bell state 4) significantly. The Bellstate in 2) was measured after these issues were fixed.

4.2 Commutation Game

The measurement of the commutation game has been done as described in section 3.6. For each pair of Pauli operator, that were set by Alice-1 and Alice-2 the coincidences Charlie-0/Bob and Charlie-1/Bob have been measured with an integration time of 60 seconds. The used waveplate settings for the Pauli operators in this experiment are:

U	QWP_1	HWP	QWP_2
$\hat{\mathcal{I}}$	0°	0°	0°
$\hat{\sigma}_x$	0°	45°	0°
$\hat{\sigma}_y$	90°	45°	0°
$\hat{\sigma}_z$	90°	0°	0°

Table 4.5: **List of waveplate settings for Alice-1 and Alice-2.** For both unitary gates U_1 and U_2, the Pauli operators were implemented using the same waveplate angles.

Every combination of Pauli operators between Alice-1 and Alice-2 has to be tested. Therefore the commutation game consists of 16 measurements that were performed in the order:

N	1	2	3	4	5	6	7	8	9	10	11	12	13	14	15	16
Alice 1	$\mathcal{I}$	$\mathcal{I}$	$\mathcal{I}$	$\mathcal{I}$	X	X	X	X	Y	Y	Y	Y	Z	Z	Z	Z
Alice 2	$\mathcal{I}$	X	Y	Z	$\mathcal{I}$	X	Y	Z	$\mathcal{I}$	X	Y	Z	$\mathcal{I}$	X	Y	Z

Table 4.6: For each measurements $N = 1 \dots 16$ Alice-1 and Alice-2 have to set a combination of two Pauli operators. Here, for better readability, $\hat{\mathcal{I}}$, $\hat{\sigma}_x, \hat{\sigma}_y$ and $\hat{\sigma}_z$ are denoted as $\mathcal{I}$, X, Y and Z.

The the channels of the function generators that control the optical switches have been adjusted to the following settings:

SG 1 (time bin switch)	Signal Hight [V]	Delay [ns]
Ch.1 (to SWITCH)	3.5	712
Ch.2 (from SWITCH)	5.0	56
SG 2 (in/out SWITCH)	Signal Hight [V]	Delay [ns]
Ch.1 (SWITCH out)	3.23	112
Ch.2 (SWITCH in)	3.2	100

Table 4.7: The voltage settings and time delays for the electrical trigger pulses, that control the optical fibre switches in the setup. Upon receiving a pulse, an optical switch transitions from the cross state to the parallel state.

Time Tagger Channel	Delay [ns]
4 (Charlie-0 H)	61.61
8 (Charlie-0 V)	60.26
17 (Charlie-1 H)	0
16 (Charlie-1 V)	6.63
14 (Bob H)	1269.11

Table 4.8: Time tagger channels and their respective time delays for the coincidence measurements for Commutation Game. Since the signal photon travels now threw the whole SWITCH-setup, Bobs detector-click must be delayed much further, then for the tomography measurements.

The probability for commuting operators is then calculated by by the sum of the coincidence counts (cc) between Bob H-path and the detectors that together form port-0 divided by the total number of coincidences between Bobs H-path and all of Charlies channels

$$P_{[U_1,U_2]} = P^0 = \frac{cc_{port0}}{cc_{total}} = \frac{cc_{V_0} + cc_{H_1}}{cc_{H_0} + cc_{V_0} + cc_{H_1} + cc_{V_1}}. \tag{4.2}$$

H_0, V_0, H_1, V_1 point here to the polarisation and weather the photon is measured in Charlie-0's or Charlie-1's tomography stage. Analogue the probability for anticommuting is given by

$$P_{\{U_1,U_2\}} = P^1 = \frac{cc_{port1}}{cc_{total}} = \frac{cc_{H_0} + cc_{V_1}}{cc_{H_0} + cc_{V_0} + cc_{H_1} + cc_{V_1}}, \tag{4.3}$$

With the probability errors

$$\Delta P^0 = \sqrt{\frac{P^0 * (1 - P^0)}{cc_{port0}}} \text{ and } \Delta P^1 = \sqrt{\frac{P^1 * (1 - P^1)}{cc_{port1}}}. \tag{4.4}$$

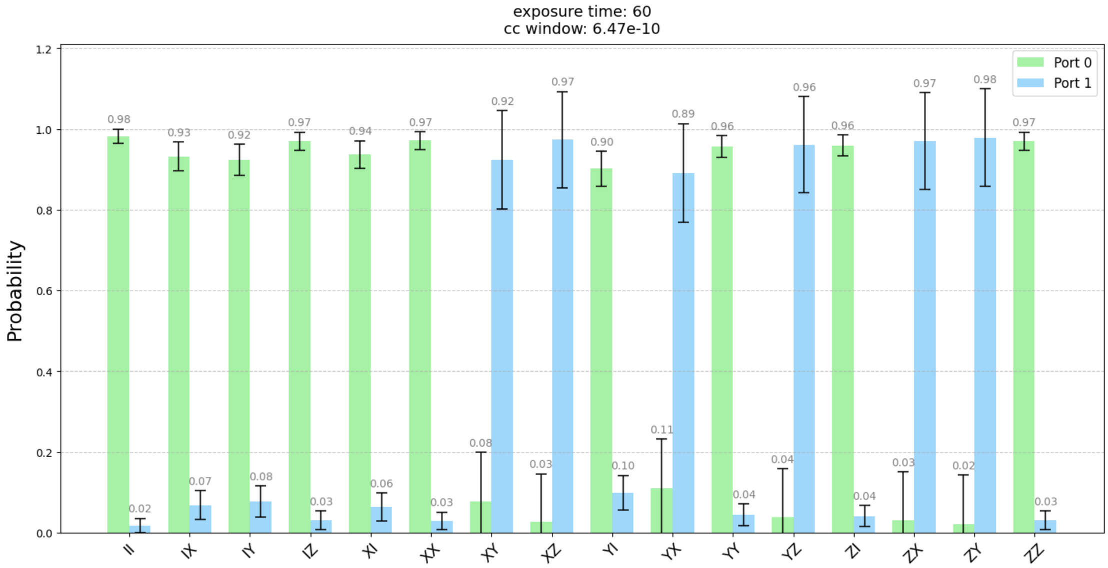

Figure 4.5: **Plotted probabilities for commuting and anticommuting operators:** The coincidences for these results were measured with an integration time of $t_{mes} = 60\ s$ and a coincidence window of $cc_{window} = 647\ ps$. When the counts appear in port-0 (given by the sum of the counts from Charlie-0's V-path and Charlie-1's H-path), the operator pair U_1, U_2, set by Alice-1 and Alice-2 in the SWITCH, commutes. When the photons end up in either Charlie-0's H-path or Charlie-1's V-path, they represent counts in port-1, which means that U_1, U_2 anticommute.

The success probability measures how well the measurements in total were able to predict, weather the Alice-1's and Alice-2's operators commuted or anticommuted. A measurement can be considered successfully if it predicted the right commutation relation with a probability > 0.5. When from a total of N measurements the commutation game determined n pairs of commuting operator pairs and m pairs of anticommuting operator correctly (with $(m+n) \leqslant N$), the success probabilities and the corresponding errors for these cases are given by

$$P^0_{succ} = \frac{1}{n}\sum_{i=1}^{n} P^0_i\ , \qquad \Delta P^0_{succ} = \sqrt{\sum_{i=1}^{n}(\Delta P^0_i)^2}\ , \tag{4.5}$$

$$P^1_{succ} = \frac{1}{m}\sum_{j=1}^{m} P^1_j\ , \qquad \Delta P^1_{succ} = \sqrt{\sum_{j=1}^{m}(\Delta P^1_j)^2}\ . \tag{4.6}$$

Here P^0_i and P^1_j are the individual probabilities out of the N measurements that fulfil $P^{0,1} > 0.5$. The total success probability of the commutation game is then calculated by

$$P_{succ} = \frac{1}{2}(P^0_{succ} + P^1_{succ})\ , \tag{4.7}$$

with an error of

$$\Delta P_{succ} = \sqrt{(\Delta P^0_{succ})^2 + (\Delta P^1_{succ})^2}. \tag{4.8}$$

For this measurements the probabilities to determine a pair of commuting operators successfully was:

$$P^0_{succ} = 0.950 \pm 0.096. \tag{4.9}$$

For anticommuting operators this probability was:

$$P^1_{succ} = 0.95 \pm 0.30. \tag{4.10}$$

This results in a total success probability of:

$$P_{succ} = 0.95 \pm 0.31 \tag{4.11}$$

5 Discussion

Overall the results presented in this thesis give good hope for a successful measurement of the local causal inequality, yet they also shows room for improvements. The results of the two qubit quantum state tomography attest, that the source creates a state with very high purity $> 99\%$ when measured between the setups of Charlie-1 and Bob and $> 97\%$ when measured between Charlie-0. With both combination a high concurrence of $c = 0.97$ was reached which will add to the chance of violating the local causal inequality. These results are not only an assurance that both of Charlie's setup operate with similar precision, it also warrants that the generated state from the SPDC source is actually the desired $|\Phi^+\rangle$ state in a quality suitable for the intended measurement of the LCI.
This is particularly applicable to the results of the commutation game measurements. It was an important step to demonstrate that the setup is capable of successfully playing the commutation game, including entanglement between the signal and idler photons for all pairs of Pauli operators. However, the measurement uncertainty for some operator pairs is still too high. The results indicate that this uncertainty especially increases when the photons end up in the detectors of Charlie-0, which occurs more frequently for anticommuting operators. This is also reflected in the size of the error in the success probability of detecting anticommuting operators, ΔP^1_{succ}, which is significantly higher than that for commuting operators, ΔP^1_{succ}.
One possible reason for this could be the coupling efficiency of Charlie-0's fiber couplers. It has been noted that it has always been more difficult to achieve proper coupling into these couplers, and this issue appeared to grow towards the end of the measurements. Additionally, it is necessary to couple these paths twice for a complete measurement. The first coupling ensures polarization compensation for the paths from the source, where the motorized mirrors direct the photons from the input coupler of the interferometer to Charlie-0's tomography stage. The second coupling is for the actual measurements, which include the quantum SWITCH. At this point, the photons arrive at the tomography stage coming from two directions through the interferometer PBS.
As a first step for the upcoming measurements, it might therefore be beneficial to reset the adjustments of all five fiber couplers involved in this process and test the transmission efficiencies of the fibres coming from Charlie-0's setup. Yet, despite these high uncertainties, the measurement of the commutation game has been successful for each operator pair.
For the results that were presented here the errors were calculated simply from shot noise and error propagation. his method places no boundaries on the maximum or minimum values, allowing the probabilities to exceed 1.0 or drop below 0.0. However, such values do not represent valid probability errors. For other publications, I would deem this method unsuitable and a Monte Carlo simulation could likely provide smaller error margins. However, since the purpose here is to give a comprehensive overview of the experiment's current status, including its existing challenges, I have chosen to present the data using

this more straightforward error method.
The final measurement of the LCI still presents several challenges. For example, we need to test whether it is safe to trigger the signal generators with a combined signal from Bob's H- and V-counts. It must be ensured that the combination of the BNC cables does not result in transients that could affect the count rate in the time tagger. Another challenge lies in the limited count rate. The optical switches operate most efficiently for single count rates of approximately 100, kHz, yet they create strong losses that result in a total single count rate of over 20, kHz, split among the four detectors of Charlie. With a heralding efficiency of the source around 15%, we end up with relatively low coincidence rates. For the measurement of the LCI, polarisation filters will be used for the measurements of Alice-1 and Alice-2, which will further decrease the count rate
Besides the experimental challenges, there are also some theoretical aspects of the experiment that should be noted. This experiment aims to provide the first device-independent evidence for the ICO in the quantum SWITCH, but it does not address the issue of ruling out potential loopholes. One significant loophole arises from the fact that, in the setup, Bob's measurement occurs earlier in time than Alice's, rather than simultaneously. As a result, one could argue that this configuration does not fully comply with the assumption of relativistic causality. Unfortunately, resolving this issue is not straightforward. The setup relies on Bob's earlier measurement to trigger the optical switches at the precise arrival time of the signal photon.
Van der Lugt et al. [1] have raised concerns in their paper regarding the violation of the LCI through a photonic quantum SWITCH. They argue that this violation can be questioned from the perspective of classical relativity theory, as the final measurement is not conducted within the quantum SWITCH itself, but only afterward, when the photons reach the detector.
In response to this concern, one might argue that it raises questions about the definition of measurement in quantum mechanics. There are valid arguments supporting the view that the application of a polarization filter in the SWITCH, as we intend to use it, effectively serves as a measurement of the quantum state as it collapses the wave function into one of its eigenstates [42, p. 172].

6 | Conclusion

List of Abbreviations

cc coincidence counts

CHSH Clauser-Horne-Shimony-Holt

CJ Choi-Jamiołkowsky

CP completely positive

CW continuous wave

DWDM dense wavelength division multiplexer

FWHM full width at half maximum

HWP half-wave plate

ICO indefinite causal order

LCI Local Causal Inequality

LP long pass

MI measurement independence

NLC nonlinear crystal

PBS polarising beam splitter

PI parameter independence

PM polarisation maintaining

QPM quasi phase matching

QC-QC Quantum Circuit with Quantum Control of causal order

QWP quarter-wave plate

SHG second harmonic generation

SNSPD superconducting nanowire single-photon detector

SPDC spontaneous parametric down-conversion

Bibliography

1. Van Der Lugt, T., Barrett, J. & Chiribella, G. Device-Independent Certification of Indefinite Causal Order in the Quantum Switch. *Nature Communications* **14,** 5811. ISSN: 2041-1723. (2024) (Sept. 2023).
2. Heisenberg, W. Zur Frage Der Kausalität in Der Quantentheorie Der Elementarteilchen. *Zeitschrift für Naturforschung A* **6,** 281–284. ISSN: 1865-7109, 0932-0784. (2024) (June 1951).
3. Oreshkov, O., Costa, F. & Brukner, Č. Quantum Correlations with No Causal Order. *Nature Communications* **3,** 1092. ISSN: 2041-1723. (2024) (Oct. 2012).
4. Procopio, L. M. *et al.* Experimental Superposition of Orders of Quantum Gates. *Nature Communications* **6,** 7913. ISSN: 2041-1723. (2024) (Aug. 2015).
5. Ebler, D., Salek, S. & Chiribella, G. Enhanced Communication with the Assistance of Indefinite Causal Order. *Physical Review Letters* **120,** 120502. ISSN: 0031-9007, 1079-7114. (2024) (Mar. 2018).
6. Goswami, K., Cao, Y., Paz-Silva, G. A., Romero, J. & White, A. G. Increasing Communication Capacity via Superposition of Order. *Physical Review Research* **2,** 033292. ISSN: 2643-1564. (2024) (Aug. 2020).
7. An, M. *et al.* Noisy Quantum Parameter Estimation with Indefinite Causal Order. *Physical Review A* **109,** 012603. ISSN: 2469-9926, 2469-9934. (2024) (Jan. 2024).
8. Araújo, M., Costa, F. & Brukner, Č. Computational Advantage from Quantum-Controlled Ordering of Gates. *Physical Review Letters* **113,** 250402. ISSN: 0031-9007, 1079-7114. (2024) (Dec. 2014).
9. Rozema, L. A. *et al.* Experimental Aspects of Indefinite Causal Order in Quantum Mechanics. *Nature Reviews Physics* **6,** 483–499. ISSN: 2522-5820. (2024) (July 2024).
10. Araújo, M. *et al.* Witnessing Causal Nonseparability. *New Journal of Physics* **17,** 102001. ISSN: 1367-2630. arXiv: `1506.03776 [quant-ph]`. (2024) (Oct. 2015).
11. Rubino, G. *et al.* Experimental Verification of an Indefinite Causal Order. *Science Advances* **3,** e1602589. ISSN: 2375-2548. (2024) (Mar. 2017).
12. Rubino, G. *et al.* Experimental Entanglement of Temporal Order. *Quantum* **6,** 621. ISSN: 2521-327X. (2024) (Jan. 2022).
13. Cao, H. *et al.* Semi-Device-Independent Certification of Indefinite Causal Order in a Photonic Quantum Switch. *Optica* **10,** 561. ISSN: 2334-2536. (2024) (May 2023).
14. Altepeter, J., Jeffrey, E. & Kwiat, P. in *Advances In Atomic, Molecular, and Optical Physics* 105–159 (Elsevier, 2005). ISBN: 978-0-12-003852-7. (2024).

15. Chiribella, G., D'Ariano, G. M., Perinotti, P. & Valiron, B. Quantum Computations without Definite Causal Structure. *Physical Review A* **88,** 022318. ISSN: 1050-2947, 1094-1622. (2024) (Aug. 2013).

16. Strömberg, T. *et al.* Experimental Superposition of Time Directions. *Physical Review Research* **6,** 023071. ISSN: 2643-1564. arXiv: `2211.01283 [quant-ph]`. (2024) (Apr. 2024).

17. Antesberger, M., Quintino, M. T., Walther, P. & Rozema, L. A. Higher-Order Process Matrix Tomography of a Passively-Stable Quantum Switch. *PRX Quantum* **5,** 010325. ISSN: 2691-3399. (2024) (Feb. 2024).

18. Wechs, J., Dourdent, H., Abbott, A. A. & Branciard, C. Quantum Circuits with Classical Versus Quantum Control of Causal Order. *PRX Quantum* **2,** 030335. ISSN: 2691-3399. (2024) (Aug. 2021).

19. Swabian_Instruments. *Time Tagger Series _Streaming Time-to-Digital Converters* 2024. (2024).

20. T&M_World. *Optical Extinction Ratio | Polarization Extinction Ratio* https://www.test-and-measurement-world.com/Terminology/What-is-Optical-Extinction-Ratio.html. 2016. (2024).

21. Neumann, S. P., Selimovic, M., Bohmann, M. & Ursin, R. Experimental Entanglement Generation for Quantum Key Distribution beyond 1 Gbit/s. *Quantum* **6,** 822. ISSN: 2521-327X. (2024) (Sept. 2022).

22. Chekhova, M. & Banzer, P. *Polarization of Light: In Classical, Quantum, and Nonlinear Optics* ISBN: 978-3-11-066801-8 (De Gruyter, Berlin Boston, 2021).

23. Strömberg, K. T. A. T. *Exploring Quantum Information with Single Photons* PhD thesis (Universität Wien, Wien, 2023). (2024).

24. Powers, P. E. & Haus, J. W. *Fundamentals of Nonlinear Optics, Second Edition* ISBN: 978-1-315-11643-3. (2024) (CRC Press, Apr. 2017).

25. Steinlechner, F. *et al.* Efficient Heralding of Polarization-Entangled Photons from Type-0 and Type-II Spontaneous Parametric Downconversion in Periodically Poled KTiOPO_4. *Journal of the Optical Society of America B* **31,** 2068. ISSN: 0740-3224, 1520-8540. (2024) (Sept. 2014).

26. Armstrong, J. A., Bloembergen, N., Ducuing, J. & Pershan, P. S. Interactions between Light Waves in a Nonlinear Dielectric. *Physical Review* **127,** 1918–1939. ISSN: 0031-899X. (2024) (Sept. 1962).

27. Boyd, R. W. *Nonlinear Optics* Fourth edition. ISBN: 978-0-12-811002-7 (Elsevier, AP Academic Press, London, 2020).

28. HC-Photonics. *PPLN Guide: Overview* https://www.hcphotonics.com/ppln-guide-overview.

29. AG, T. P. *Toptica Laser -Production and Quality Control Sheet*

30. Senior, J. M. & Jamro, M. Y. *Optical Fiber Communications: Principles and Practice* 3rd ed. ISBN: 978-0-13-032681-2 (Financial Times/Prentice Hall, Harlow, England ; New York, 2009).

31. Donohue, J. M., Agnew, M., Lavoie, J. & Resch, K. J. Coherent Ultrafast Measurement of Time-Bin Encoded Photons. *Physical Review Letters* **111,** 153602. ISSN: 0031-9007, 1079-7114. (2024) (Oct. 2013).

32. Strömberg, T., Schiansky, P. & Walther, P. Prescriptive Method for Fiber Polarization Compensation in Two Bases. *Applied Optics* **63,** 1822. ISSN: 1559-128X, 2155-3165. (2024) (Mar. 2024).

33. thorlabs inc. *Fiber_ Polarization_ Controller_ Lab_ Facts* (2024).

34. Antesberger, M. *et al.* Distribution of Telecom Entangled Photons through a 7.7 Km Antiresonant Hollow-Core Fiber. *Optica Quantum* **2,** 173. ISSN: 2837-6714. (2024) (June 2024).

35. Lambropoulos, P. & Petrosyan, D. *Fundamentals of Quantum Optics and Quantum Information* ISBN: 978-3-540-34571-8 (Springer, Berlin ; New York, 2007).

36. Nielsen, M. A. & Chuang, I. L. *Quantum Computation and Quantum Information* 10th anniversary ed. ISBN: 978-1-107-00217-3 (Cambridge University Press, Cambridge ; New York, 2010).

37. Bertlmann, R. A. & Friis, N. *Theoretical Physics T2 Quantum Mechanics, Course of Lectures by Reinhold A. Bertlmann at the University of Vienna* Wien, 2008. (2024).

38. Hill, S. & Wootters, W. K. Entanglement of a Pair of Quantum Bits. *Physical Review Letters* **78,** 5022–5025. ISSN: 0031-9007, 1079-7114. (2024) (June 1997).

39. Wootters, W. K. Entanglement of Formation of an Arbitrary State of Two Qubits. *Physical Review Letters* **80,** 2245–2248. ISSN: 0031-9007, 1079-7114. (2024) (Mar. 1998).

40. James, D. F. V., Kwiat, P. G., Munro, W. J. & White, A. G. Measurement of Qubits. *Physical Review A* **64,** 052312. ISSN: 1050-2947, 1094-1622. (2024) (Oct. 2001).

41. Kwiat-Quantum-Information-Group. *Documentation: Python Tomography Libary* https://quantumtomo.web.illinois.edu/Doc/. 2024. (2024).

42. Zettili, N. *Quantum Mechanics: Concepts and Applications* Repr. ISBN: 978-0-471-48944-3 978-0-471-48943-6 (Wiley, Chichester Weinheim, 2008).

43. D'Ariano, G. M., Leonhardt, U. & Paul, H. Homodyne Detection of the Density Matrix of the Radiation Field. *Physical Review A* **52,** R1801–R1804. ISSN: 1050-2947, 1094-1622. (2024) (Sept. 1995).

44. D'Ariano, G. M., Paris, M. G. A. & Sacchi, M. F. Quantum Tomography. (2024) (2003).

45. DeCusatis, C. in *Handbook of Fiber Optic Data Communication* 55–76 (Elsevier, 2013). ISBN: 978-0-12-401673-6. (2024).

List of Figures

List of Tables

A | The (Z+X) and the (Z-X) Basis

A.1 The (Z+X) Basis

The sum of the Pauli operators $\hat{\sigma_x}$ and $\hat{\sigma_z}$ gives the matrix $\hat{A}^+$

$$\hat{A}^+ = \hat{\sigma_z} + \hat{\sigma_x} = \begin{pmatrix} 1 & 0 \\ 0 & -1 \end{pmatrix} + \begin{pmatrix} 0 & 1 \\ 1 & 0 \end{pmatrix} = \begin{pmatrix} 1 & 1 \\ 1 & -1 \end{pmatrix}, \tag{A.1}$$

with normalized eigenvectors:

$$\begin{aligned} v_1^+ &= \frac{\sqrt{2-\sqrt{2}}}{2} \begin{pmatrix} \sqrt{2}+1 \\ 1 \end{pmatrix} = \begin{pmatrix} \frac{\sqrt{2+\sqrt{2}}}{2} \\ 0 \end{pmatrix} + \begin{pmatrix} 0 \\ \frac{\sqrt{2-\sqrt{2}}}{2} \end{pmatrix}, \\ v_2^+ &= \frac{\sqrt{2+\sqrt{2}}}{2} \begin{pmatrix} -\sqrt{2}+1 \\ 1 \end{pmatrix} = \begin{pmatrix} \frac{\sqrt{-2-\sqrt{2}}}{2} \\ 0 \end{pmatrix} + \begin{pmatrix} 0 \\ \frac{\sqrt{2+\sqrt{2}}}{2} \end{pmatrix}. \end{aligned} \tag{A.2}$$

Thus the eigenstates of this basis can be written in the $|H/V\rangle$ basis as

$$\begin{aligned} |0\rangle_{Z+X} &= \frac{1}{2}\left(\sqrt{2+\sqrt{2}}\,|H\rangle + \sqrt{2+\sqrt{2}}\,|V\rangle\right), \\ |1\rangle_{Z+X} &= \frac{1}{2}\left(-\sqrt{2-\sqrt{2}}\,|H\rangle + \sqrt{2+\sqrt{2}}\,|V\rangle\right). \end{aligned} \tag{A.3}$$

A.2 The (Z-X) Basis

Subtracting the Pauli operators $\hat{\sigma_x}$ from $\hat{\sigma_z}$ gives the matrix $\hat{A}^-$

$$\hat{A}^- = \hat{\sigma_z} - \hat{\sigma_x} = \begin{pmatrix} 1 & 0 \\ 0 & -1 \end{pmatrix} - \begin{pmatrix} 0 & 1 \\ 1 & 0 \end{pmatrix} = \begin{pmatrix} 1 & -1 \\ -1 & -1 \end{pmatrix}, \tag{A.4}$$

with normalized eigenvectors:

$$\begin{aligned} v_1^- &= \frac{\sqrt{2+\sqrt{2}}}{2} \begin{pmatrix} \sqrt{2}-1 \\ 1 \end{pmatrix} = \begin{pmatrix} \frac{\sqrt{2-\sqrt{2}}}{2} \\ 0 \end{pmatrix} + \begin{pmatrix} 0 \\ \frac{\sqrt{2+\sqrt{2}}}{2} \end{pmatrix}, \\ v_2^- &= \frac{\sqrt{2-\sqrt{2}}}{2} \begin{pmatrix} -\sqrt{2}-1 \\ 1 \end{pmatrix} = \begin{pmatrix} \frac{-\sqrt{2+\sqrt{2}}}{2} \\ 0 \end{pmatrix} + \begin{pmatrix} 0 \\ \frac{\sqrt{2-\sqrt{2}}}{2} \end{pmatrix}. \end{aligned} \tag{A.5}$$

Thus the eigenstates of this basis can be written in the $|H/V\rangle$ basis as

$$
\begin{aligned}
|0\rangle_{Z-X} &= \frac{1}{2}\left(-\sqrt{2+\sqrt{2}}\,|H\rangle + \sqrt{2+\sqrt{2}}\,|V\rangle\right), \\
|1\rangle_{Z-X} &= \frac{1}{2}\left(\sqrt{2-\sqrt{2}}\,|H\rangle + \sqrt{2+\sqrt{2}}\,|V\rangle\right).
\end{aligned} \tag{A.6}
$$

B Tables

DWDM-Channel	λ [nm] $\pm 0.020\ nm$	Degree of Polarisation $\pm$ 1.0 %
C32	1551.720	100.0 %
C33	1550.920	99.9 %
C35	1549.320	100.0 %
C36	1548.510	98.9 %

Table B.1: The four DWDM channels, with their respective wavelengths, were measured for their degree of polarisation. The tunable alignment laser was connected to the DWDM and set to the wavelength of each output channel, the degree of polarisation was measured with a Thorlabs polarimeter PAX1000IR2. The results show that the DWDM does not compromise the purity of the polarisation states.

λ [nm] ($\pm$ 0.02 nm)	1552.52 (C31)	1551.72 (C32)	1550.92 (C33)	1550.12 (C34)
C32	52.5 nW $\pm$ 1.6 nW	3.72 mW $\pm$ 0.12 mW	0.0900 nW $\pm$ 0.0027 nW	
C33		55.50 nW $\pm$ 0.17 nW	4.00 mW $\pm$ 0.12 mW	9.67 nW $\pm$ 0.30 nW

λ [nm] ($\pm$ 0.02 nm)	1550.12 (C34)	1549.32 (C35)	1548.51 (C36)	1547.72 (C37)
C35	33.1 nW $\pm$ 1.0 nW	4.12 mW $\pm$ 0.13 mW	0.1100 nW $\pm$ 0.033 nW	
C36		4.10 nW $\pm$ 0.13 nW	1.000 mW $\pm$ 0.030 mW	4.80 nW $\pm$ 0.15 nW

Table B.2: Measurement of the power leakage into the DWDM channels from the wavelengths of neighbouring channels. For this, the tunable alignment laser was connected to the DWDM input fibre, set to the transmission wavelength of the respective channel. The power of this channel and the two neighbouring channels was then measured. As shown here, the leakage into the neighbouring channels is negligibly small.

$\|HH\rangle$	HH	HV	VH	VV
HH	0.9275 $+ 0.0i$	-0.1848 $+ 0.1702i$	0.0398 $- 0.0481i$	-0.00998 $+ 0.0108i$
HV	-0.1848 $- 0.1702i$	0.0681 $+ 0.0i$	-0.0168 $+ 0.0023i$	0.0040 $- 0.0003i$
VH	0.0398 $+ 0.0481i$	-0.0168 $- 0.0023i$	0.0042 $+ 0.0i$	-0.00099 $- 0.0000528i$
VV	-0.00998 $- 0.0108i$	0.0040 $+ 0.0003i$	-0.00099 $+ 0.0000528i$	0.0003 $+ 0.0i$

$\|\Phi^-\rangle$	HH	HV	VH	VV
HH	0.5085 $+ 0.0i$	-0.1037 $+ 0.0892i$	0.0452 $+ 0.0173i$	-0.4132 $- 0.0224i$
HV	-0.1037 $- 0.0892i$	0.0934 $+ 0.0i$	-0.0127 $+ 0.0001i$	0.0593 $+ 0.0262i$
VH	0.0452 $- 0.0173i$	-0.0127 $- 0.0001i$	0.0077 $+ 0.0i$	-0.0455 $+ 0.0222i$
VV	-0.4132 $+ 0.0224i$	0.0593 $- 0.0262i$	-0.0455 $- 0.0222i$	0.3904 $+ 0.0i$

$\|VV\rangle$	HH	HV	VH	VV
HH	0.0008 $+ 0.0i$	-0.0012 $- 0.0016i$	-0.0039 $- 0.0031i$	0.0182 $- 0.0079i$
HV	-0.0012 $+ 0.0016i$	0.0073 $+ 0.0i$	0.0063 $- 0.0051i$	0.0062 $+ 0.0317i$
VH	-0.0039 $+ 0.0031i$	0.0063 $+ 0.0051i$	0.0583 $+ 0.0i$	-0.1096 $+ 0.2058i$
VV	0.0182 $+ 0.0079i$	0.0062 $- 0.0317i$	-0.1096 $- 0.2058i$	0.9337 $+ 0.0i$

Table B.3: Tables with the numeric results for three of the density density matrices shown in figure 4.4. The fourth equals the matrix between Bob and Charlie 1, displayed in the table below.

	HH	HV	VH	VV
HH	$0.4627 + 0.0i$	$-0.0159 - 0.0151i$	$0.0586 - 0.0046i$	$0.4823 - 0.0191i$
HV	$-0.0159 + 0.0151i$	$0.0055 + 0.0i$	$-0.0047 + 0.0038i$	$-0.0246 + 0.0138i$
VH	$0.0586 + 0.0046i$	$-0.0047 - 0.0038i$	$0.0100 + 0.0i$	$0.0659 + 0.0074i$
VV	$0.4823 + 0.0191i$	$-0.0246 - 0.0138i$	$0.0659 - 0.0074i$	$0.5218 + 0.0i$

Table B.4: table of the numeric values of the density matrix of the $|\Phi^+\rangle$ state between Charlie-0 and Bob, corresponding to the figure 4.2

	HH	HV	VH	VV
HH	$0.6021 + 0.0i$	$0.0339 + 0.0190i$	$-9.0944 \cdot 10^{-5} - 0.0022i$	$0.4856 + 0.0118i$
HV	$0.0339 - 0.0190i$	$0.0028 + 0.0i$	$0.0003 + 0.0007i$	$0.0279 - 0.0151i$
VH	$-9.0944 \cdot 10^{-5} + 0.0022i$	$0.0003 - 0.0007i$	$0.0026 + 0.0i$	$-0.0010 + 0.0008i$
VV	$0.4856 - 0.0118i$	$0.0279 + 0.0151i$	$-0.0010 - 0.0008i$	$0.3925 + 0.0i$

Table B.5: table of the numeric values of the density matrix of the $|\Phi^+\rangle$ state between Charlie-1 and Bob, corresponding to the figure 4.3.

Operator Set	Ch0_H	Ch0_V	Ch1_H	Ch1_V
II	0.25 ± 0.51	0.68 ± 0.83	57.1 ± 7.6	0.80 ± 0.85
IX	3.1 ± 1.8	46.3 ± 6.9	4.0 ± 2.1	0.62 ± 0.79
IY	3.6 ± 1.9	47.3 ± 6.9	0.05 ± 0.23	0.32 ± 0.57
IZ	1.3 ± 1.2	3.2 ± 1.8	53.9 ± 7.3	0.48 ± 0.70
XI	3.4 ± 1.9	47.9 ± 7.0	2.3 ± 1.5	0.03 ± 0.19
XX	0.85 ± 0.93	2.1 ± 1.5	57.5 ± 7.6	0.92 ± 0.96
XY	2.5 ± 1.6	0.27 ± 0.52	4.5 ± 2.2	54.5 ± 7.4
XZ	66.2 ± 8.2	0.79 ± 0.89	1.0 ± 1.1	0.67 ± 0.82
YI	3.8 ± 2.0	46.9 ± 6.9	0.50 ± 0.71	1.3 ± 1.2
YX	4.6 ± 2.2	1.5 ± 1.3	5.0 ± 2.3	48.2 ± 7.0
YY	0.45 ± 0.68	0.67 ± 0.82	56.4 ± 7.6	2.2 ± 1.5
YZ	60.5 ± 7.8	0.95 ± 0.98	1.7 ± 1.3	4.5 ± 2.2
ZI	1.4 ± 1.2	1.8 ± 1.4	55.1 ± 7.5	1.0 ± 1.1
ZX	64.3 ± 8.1	1.1 ± 1.1	0.92 ± 0.96	0.99 ± 1.0
ZY	61.4 ± 7.9	1.3 ± 1.2	0.17 ± 0.41	3.6 ± 1.9
ZZ	1.2 ± 1.2	1.0 ± 1.1	55.5 ± 7.5	0.58 ± 0.77

Table B.6: Measured coincidence rates for the commutation game state between Charlie-0 and Bob